Multiscale Tortuous Diffusion in Anion- and Cation-Exchange Membranes: Exploration of Counterions, Water Content, and Polymer Functionality

Lam M. Thieu

Thesis submitted to the faculty of the

Virginia Polytechnic Institute and State University

in partial fulfillment of the requirements for the degree of

Master of Science
in
Macromolecular Science and Engineering

Louis A. Madsen, Chair

Harry C. Dorn

Paul A. Deck

August 9, 2017
Blacksburg, Virginia

Keywords: fuel cell, ion-exchange membranes, AEMs, PFG-NMR, self-diffusion, restricted diffusion

Multiscale Tortuous Diffusion in Anion- and Cation-Exchange Membranes: Exploration of Counterions, Water Content, and Polymer Functionality

Lam M. Thieu

Abstract: Fundamental understanding of water transport and morphology is critical for improving ion conductivity in polymer electrolyte membranes (PEMs). Herein, we present comprehensive water transport measurements comparing anion-exchange membranes (AEMs) based on ammonium-functionalized poly(phenylene oxide) and cation-exchange membranes (CEMs) based on sulfonated poly(ether sulfone). We investigate the influence of counter ions, alkyl side chain, and degree of functionalization on water transport in AEMs and CEMs using pulsed-field-gradient (PFG) NMR diffusometry. Water diffusion in both AEMs and CEMs exhibit specific trends as a function of water uptake (wt%), indicating morphological similarities across common chemical structures. Furthermore, restricted diffusion reveals micron-scale heterogeneity of the hydrophilic network in both CEMs and AEMs. We propose a model wherein the hydrophilic network in these membranes has micron-scale distributions of local nm-scale dead ends, leading to changes in tortuosity as a function of water content, counterion type, and polymer structure. We furthermore parse tortuosity into two regimes, corresponding to nm-to-bulk and μm-to-bulk ranges, which reveal the importance of multi-scale morphological structures that influence bulk transport. This study provides new insights into polymer membrane morphology from nm to μm scales with the ultimate goal of controlling polymeric materials for enhanced fuel cells and other separations applications.

Multiscale Tortuous Diffusion in Anion- and Cation-Exchange Membranes: Exploration of Counterions, Water Content, and Polymer Functionality

Lam M. Thieu

General Audience Abstract: Using clean energy in place of fossil fuels to reduce carbon dioxide emissions is one of the biggest challenges of the 21st century. Among emerging technologies, fuel cells (FCs) show tremendous potential to be a candidate for the energy of the future. An FC is "an electrochemical device that directly converts chemical energy into electrical energy" with the only byproduct being heat and water. The key component of an FC is a polymer-electrolyte membrane, which helps to separate electrons and fuel and allows ions to move through. The current commercial membranes, named cation-exchange membranes (CEMs), employ precious metals such as platinum (Pt) as a catalyst, significantly increasing the cost. Anion exchange membranes (AEMs) are another alternative currently being investigated to reduce the cost of FCs because they can employ cheaper catalysts such as nickel or silver. This thesis investigated the motion of water inside AEMs and CEMs, and proposed a model to explain how water transports in these membranes. The result of this study provides new insights into polymer membrane internal structure with the ultimate goal of controlling polymeric materials for enhanced fuel cells and other separations applications such as reverse-osmosis water purification.

Acknowledgements

First and foremost, I want to send a special thanks to my advisor, Dr. Louis. A. Madsen. He allowed me to join his group two years ago and provided me tremendous support and opportunities. I have learned many things from him, not only regarding research and advanced knowledge but also the fundamental value of a scientist. This work would have been impossible without his constant support. It is my best luck to be one of his mentees.

I also appreciate my remaining thesis committee, Dr. Paul Deck, and Dr. Harry Dorn for inspiring and supporting me to finish my study. Dr. Deck also helped me with some sample manipulations that required anaerobic techniques and provided detail comments for my thesis.

Moreover, I am grateful for the support from my lab mates for my research. I also want to thank my Vietnamese friends in Blacksburg, who always stay with me and share unforgettable memories.

My family plays an important role for the success of my study. I want to express gratitude for my parents, my sister, and my fiancé for their unconditional love and constant support. My study would be extremely harder if I do not have their support.

Finally, I want to thank Vietnam Education Foundation (VEF) for giving me a chance to study in the US. It will be one of the most memorial experiences I have ever had.

Attribution

Chapter 2 of this Thesis describes the main body of my work and will be soon submitted to a peer-reviewed journal, most likely *Macromolecules*. In this attribution section, I acknowledge contributions made by others to this work.

Liang Zhu, PhD (Dr. Michael Hickner's Lab, Department of Materials Science and Engineering, Pennsylvania State University) is currently a postdoctoral research associate at Pennsylvania State University. Dr. Zhu was a coauthor on this paper and synthesized the AEMs and CEMs used in this study and will be a co-author of the ensuing manuscript.

Andrew Korovich (Dr. Louis Madsen's Lab, Department of Chemistry) is currently a Ph.D. student at Virginia Tech. Mr. Korovich contributed to the dead end, swelling, and tortuosity model and will be a co-author of the ensuing manuscript.

Michael A. Hickner, Ph.D. (Faculty Member, Department of Materials Science and Engineering, Pennsylvania State University) is currently an associate professor in the Department of Materials Science and Engineering at Pennsylvania State University. Dr. Hickner provided deep discussions on understanding the data and will be a co-author of the ensuing manuscript.

Louis A. Madsen, Ph.D. (Faculty Member, Department of Chemistry) is currently an associate professor in the Chemistry Department at Virginia Tech. Dr. Madsen, committee chair for this thesis, was a co-author on this paper, providing substantial editing of this document as well as deep discussions on understanding the data.

Table of content

List of Figures

Chapter 1: Introduction

1.1. Polymer electrolyte membranes for alternative energy

Using clean energy in place of fossil fuels to reduce carbon dioxide emissions is one of the biggest challenges of the 21st century. Among emerging technologies, fuel cells (FCs) show tremendous potential to be a candidate for the energy of the future because a FC can act as a zero-emission converter and is not limited by the Carnot cycle.[1] FCs can be classified by the operating temperature as low (< 100 °C), medium (100 – 200 °C), and high (500-1000 °C).[2] Low-temperature FCs could offer an attractive alternative for producing power that is safe and environmentally friendly for vehicles.[3] The US Department of Energy (DoE) recently estimated the current price of an 80 kW automotive polymer electrolyte membrane (PEM) FC at $53/kW if scaled up to 500,000 units/year as shown in Figure 1.1.[4] The aim is to reduce the cost of FCs to $40/kW by 2020 and eventually to $30/kW.[4]

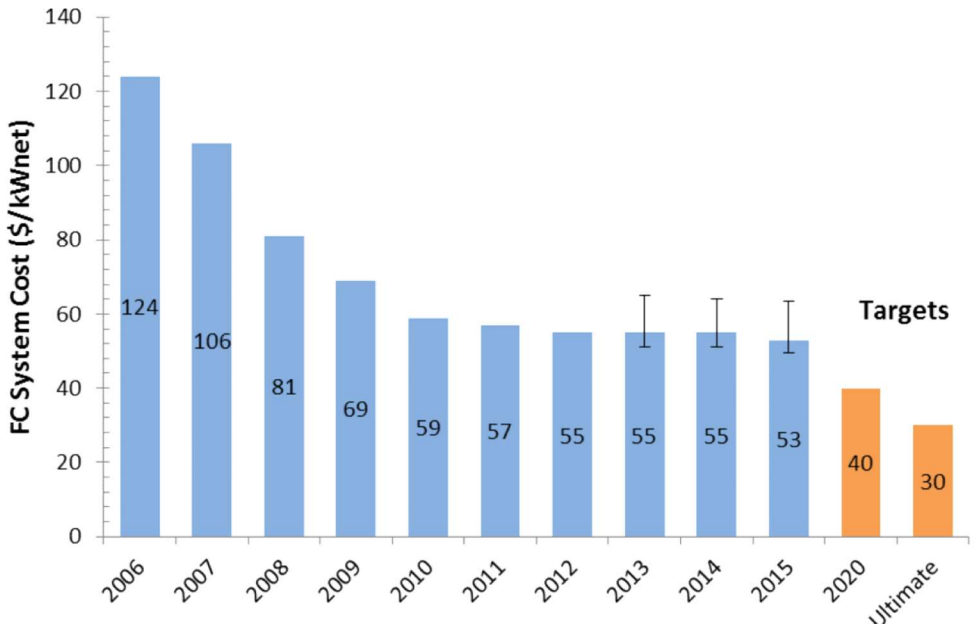

Figure 1.1. The current price of an 80 kW automotive polymer- electrolyte -membrane (PEM) FC if scaled up to 500,000 units/year from 2006 to 2015 (reproduced from 2015 Annual Report of DOE Hydrogen and Fuel Cells Program).[4]

A FC is defined as "an electrochemical device that directly converts chemical energy into electrical energy" with the only byproduct being heat.[5] FCs use fuels such as H_2, CH_3OH, N_2H_4, NH_3, and the typical oxidant is O_2.[2] The most popular commercial low-temperature FC technology currently available uses cation-exchange membranes (CEMs). The basic design of CEMs is shown schematically in Fig. 1.2, in which two electrodes are separated by an ion-exchange membrane and are connected to an external load. The common purpose of the membrane is to conduct ions and water as well as to prevent electrons and fuel gas crossing over from anode to cathode. Theoretically, a single H_2/O_2 FC shows a cell voltage of 1.2 V and one can achieve higher voltages by stacking individual cells in series.[6] CEMs employ precious metal catalysts such as Pt to turn pure hydrogen into protons, which dramatically increases the ultimate cost of PEM FCs.[7] These

considerations lead to a plateau in the cost of an FC system in recent years.[8] As shown in Figure 1.1, from 2006 to 2010, the price of an FC system had decreased from \$124/kW_{net} to \$59/kW_{net} however, in the period from 2010 to 2015; the price had just slightly reduced from \$59/kW_{net} to \$53/kW_{net}.[4]

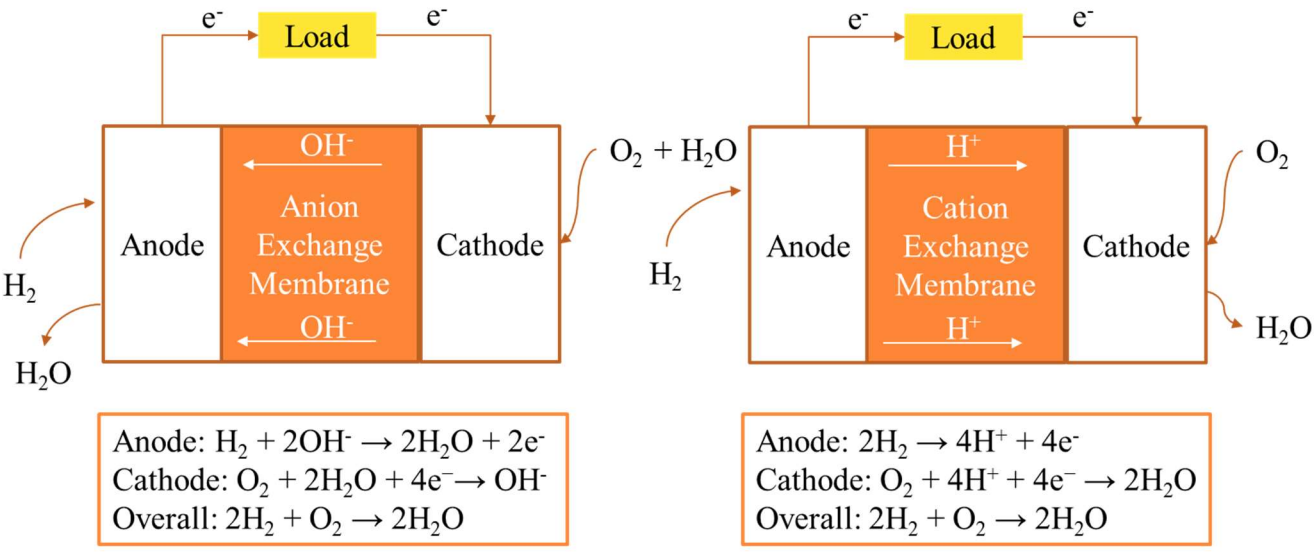

Figure 1.2. Schematics of anion exchange membrane (AEM) fuel cell (left) and cation exchange membrane (CEM) fuel cell (right).

Another type of polymer electrolyte is an anion exchange membrane (AEM). The basic design of an AEM is similar to a CEM, and it includes cathode, anode, external load and a separating membrane. However, in AEMs, hydroxide ions are transported from cathode to anode, while in CEMs, protons are transported from anode to cathode, as shown in Figure 1.2. AEMs have received much attention from the scientific community recently because they can employ cheaper metals, such as nickel or silver, which helps to decrease the ultimate price of FCs. [9-12]

Despite considerable research effort, AEMs are far from being a suitable substitute for CEMs. First, AEMs have lower conductivity than CEMs, leading to the comparatively lower performance of AEM FCs. Since the conductivity of H^+ is twice as high as the conductivity of OH^- ions in water, a twofold rise in OH^- ion concentration, or other improvements in OH- transport, is necessary to obtain similar performance.[13] Second, AEMs are insufficiently chemically and mechanically stable compared to CEMs due to the elevating operating temperature and strong alkalinity of AEM-based FCs.[14] Third, AEMs are easily degraded by CO_2 in the air since hydroxide can form carbonate or bicarbonate within the catalyst layer and AEMs, which causes a decrease in conductivity of the membrane.[15] More research is needed to advance AEMs to meet all the requirements of practical fuel cells and bring the cost below that of CEMs.

1.2. Requirements for the use of PEMs in fuel cells

Ion transport

Ion transport is the most important characteristic of PEMs. Transport rates relate to ion exchange capacity (IEC), water sorption, and morphology of the membrane. The IEC of a membrane, which equals the reciprocal value of the equivalent weight, is defined as the dry mass of polymer per mole of ionic groups (H^+ or OH^-).[2] Higher IEC values often lead to faster ion transport or conductivity; nevertheless, IEC does not indicate the dissociation of the counterion from the polymer backbone.[2] Water sorption is another influential factor contributing to ion transport because the acidic or basic groups in PEMs have to dissociate proton or hydroxide to exchange ion. Although high water content can lead to an increase of the ion transport, too much water absorption can also lead to swelling, which degrades the mechanical properties of the membrane.[16] Therefore, the "perfect" membrane should absorb less water but still efficiently transport water

and ions. This means that a membrane must possess a superior morphology with good nanophase separation between the hydrophobic matrix and hydrophilic network to conduct water and ions. For example, Nafion® only absorbs maximum 25 wt% water content; however, the diffusion coefficient of water inside Nafion can reach 6 x 10^{-10} m^2/s,[17] which is very high relative to other PEMs, due to its superior morphology with well-separated hydrophilic channels.[18-20]

Water management and water transport

Water management and water transport are two important topics in FCs, and they can easily be misleading. Water management refers to maintaining an appropriate water content in an operating FCs, which prevents the anode and membrane from dehydrating and the cathode from flooding.[21] Water transport, on the other hand, indicates how water travels through the PEM. Water transport mechanisms in PEMs involve diffusion, hydraulic permeation, and electroosmotic drag.[22] An understanding of water transport is essential for water management, which helps to keep the membrane moist and ensure the fuel cells operate efficiently. Water transport is the main topic of this study.

Chemical stability

The chemical stability of PEMs is of importance because a FC must operate up to temperatures around 90 °C and in strongly acidic or basic environment.[14] Perfluorinated sulfonic acid (PFSA) CEMs such as Nafion® and Flemion® possess excellent chemical stability that can withstand thousands of hours in an acidic environment.[23] Researchers are currently struggling to find an AEM with excellent chemical stability that can endure a long time in a basic environment at high temperature.[24-26]

Mechanical integrity

The loss of the mechanical integrity of PEMs in FCs can be caused by gas crossover, chemical degradation, or fatigue failure after repeated mechanical swelling with water during FC cycling.[27-28] Pin-hole formation or rupture of PEMs is catastrophic for FCs.[29] Although the mechanical integrity of PEM is critical, it is beyond the scope of this study.

Cost

Finally, the cost of PEMs is a major factor in commercializing FCs. The most popular type of PEM currently is the perfluorinated sulfonic acid (PFSA) CEMs, e.g., Nafion®, Flemion®, Aciplex®, which are very costly because of the complex synthesis of fluorine chemistry.[30] Furthermore, CEMs use the precious catalyst, Pt, which skyrockets the ultimate price of fuel cells. Numerous studies are focused on developing low Pt content catalysts by taking advantage of Pt nano catalysts. In addition to catalyst research for CEMFCs, anion exchange membranes (AEMs), which can employ cheaper catalyst metals, such as nickel or silver, are currently being investigated to reduce the cost of FCs.

1.3. Using NMR to study water diffusion in PEMs.

1.3.1. General remarks on nuclear magnetic resonance (NMR)

The key feature of NMR is it utilizes magnetic resonance of nuclear spin (I), which is an intrinsic property of atomic nuclei. If nuclei have spin I, it will have 2I + 1 degenerate state. When we applied an external magnetic field to the interest nuclei, its spin states will split into 2I+1 states, which commonly known as Zeeman splitting. In the presence of the magnetic field, the NMR active nuclei precess around the applied magnetic field direction (z-direction) at the Larmor frequency as shown in Eq. 1.1.[31]

$$\omega^0 = -\gamma B^0 \qquad 1.1$$

For example, if I = ½, there will be two energy state corresponding to spin up (↑) (α) and spin down (↓) (β) (up and down are relative to magnetic field direction) as shown in Figure 1.3

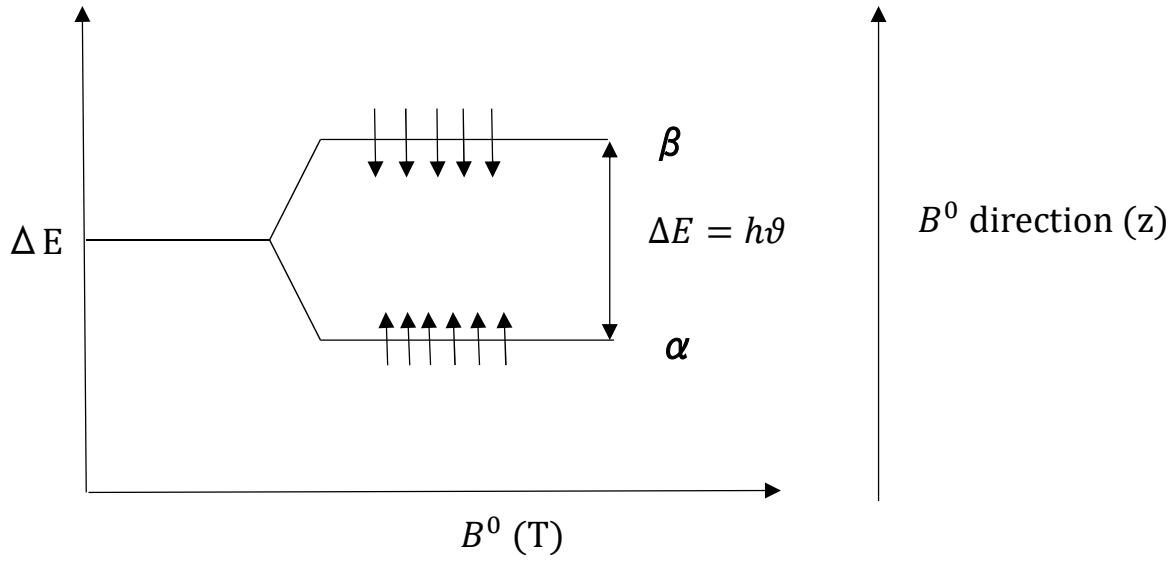

Figure 1.3. Zeeman splitting of a common spin-1/2 nucleus. When we applied an external magnetic field to the interest nuclei, its spin splits into two states: spin up (α) and spin down (β).

An important question raising is the distribution between spin up and spin down. In the absence of a magnetic field, there is no preference between spin up and spin down. However, when we applied a magnetic field to the nuclei, the number of spins up exceeds the number of spins down by a small ratio as shown in Eq. 1.2.[32]

$$\frac{N_\alpha}{N_\beta} = \exp(\frac{h\gamma B}{2\pi kT}) \qquad 1.2$$

The slight excess ratio between spin up and spin down is known as spin polarization. The net spins precess around magnetic field direction and gradually build up longitudinal nuclear spin magnetization. The characteristic time to attain the spin polarization as well as create longitudinal nuclear spin magnetization is called spin-lattice relaxation time or T_1.[32] Nonetheless, the longitudinal magnetization is too small to detect. Instead of measuring longitudinal nuclear spin magnetization, scientists tend to measure transverse magnetization by applying a rf pulse with well-defined frequency to turn the net spin magnetization along the transverse plane. Usually, we use 90° rf pulses to exclude the precession of the spin around the magnetic field direction. After applying 90° rf pulses, the spin starts to dephasing in the transverse plane (x-y plane) due to the inhomogeneity of the magnetic field.[31] The relaxation time along the transverse plane is called T_2 or spin-spin relaxation time. The transverse magnetization also is detected by rf coil, converted to an electric signal and eventually Fourier transformed (FT) to get an NMR spectrum as we can see in Figure 1.4

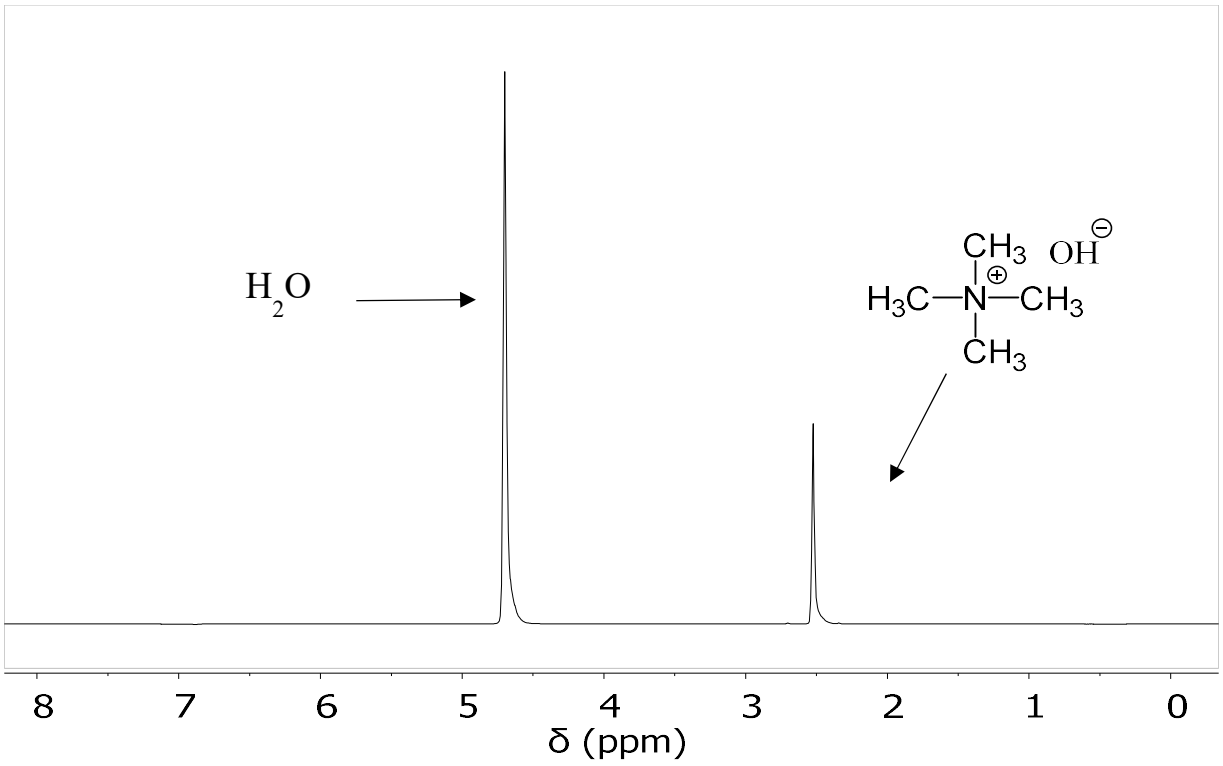

Figure 1.4. An example of a typical FT-NMR proton spectra. In the spectrum, tetramethyl ammonium hydroxide and water correspond to single peaks at 2.42 ppm and 4.7 ppm respectively.

In general, the principle of NMR can be summarized in two main steps:

Step 1: The polarization of nuclear spin along magnetic field (B_0) after spin-lattice relaxation time

Step 2: The net magnetic moment is rotated into the x-y plane by applying rf pulse. The transverse magnetization is detected by rf coil and FT to get NMR spectrum.

1.3.2. Pulsed-field-gradient (PFG) NMR diffusometry

Diffusion is one of the vital transport processes in chemical and biological systems. According to Fick's law, diffusion flux is proportional to the concentration gradient.[33] Self-diffusion coefficient, on the other hand, is the Brownian motion of molecules when the chemical potential gradient is

zero.[34] The self-diffusion coefficient of molecules is essential because it relates to many other physical properties of the system such as viscosity, hydrodynamic radius, electrophoretic mobility as shown in Eq. 1.3 and 1.4.[35]

$$D = \frac{k_B T}{6\pi\eta r} \quad 1.3$$

$$D = \frac{\mu_q k_B T}{q} \quad 1.4$$

(D is diffusion coefficient; k_B is Boltzmann's constant, T is absolute temperature, η is viscosity, r is hydrodynamic radius, μ_q is electrophoretic mobility, q is charge of the particle)

The self-diffusion coefficient can be measured by pulsed-field-gradient (PFG) NMR diffusometry. However, before talking about PFG NMR diffusometry, we have to understand the mechanism of the spin echo. Erwin Hahn first discovered the spin echo (or Hahn echo) in 1950.[36] As mentioned in the previous section, when we apply a magnetic field, the net spin polarizes along the direction of the magnetic field (or z-direction). A 90° pulse is applied along the x-direction to rotate the net spin into the x-y plane. After a period τ, each spin starts to fan out slowly or diphase. After a 180° pulse is applied along the x-axis, and then after a period τ, the net spin refocuses, and we see an "echo." All the process is illustrated in Figure 1.5.[32]

a)

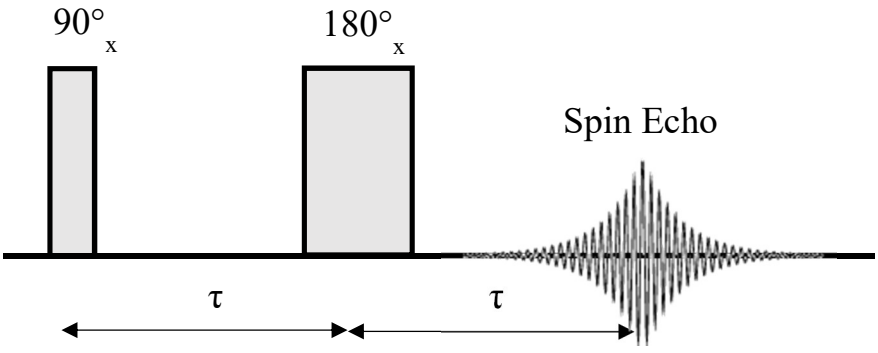

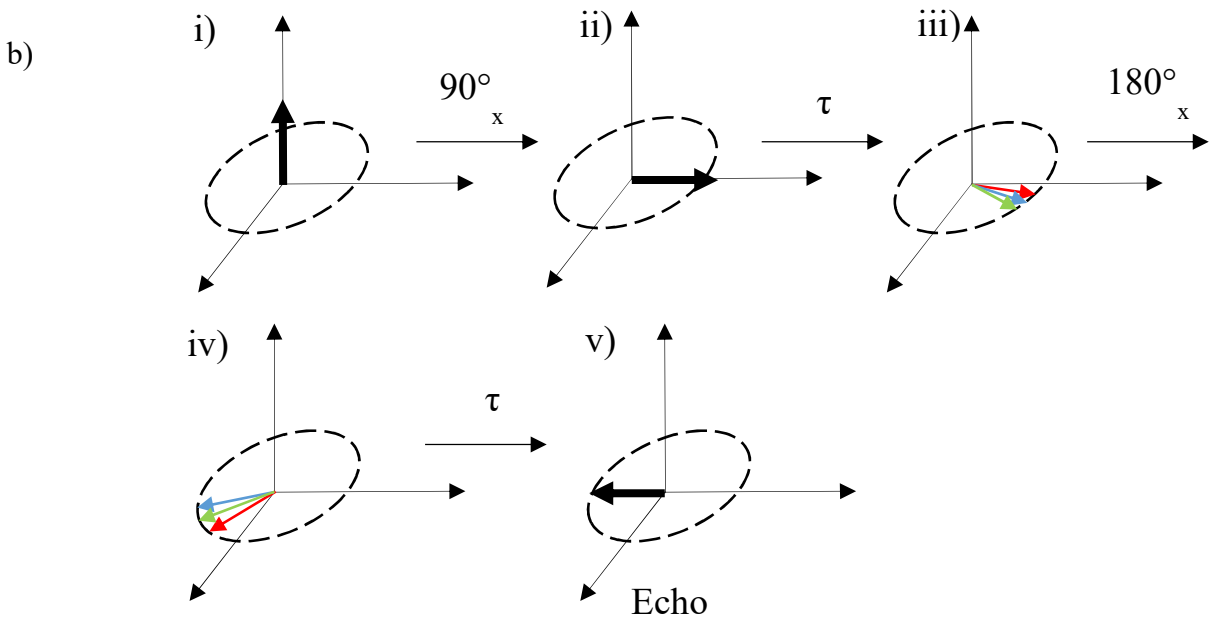

Figure 1.5. The spin echo pulse sequence in an inhomogeneous magnetic field a) rf pulse of spin echo. A 90° pulse and an 180° pulse, both along the x-axis, are applied b) the precession of net spin during spin echo. A 90° pulse is applied along the x-direction to rotate the net spin into the x-y plane. After a period τ, each spin starts to fan out slowly or dephase. After a 180° pulse is applied along the x-axis, and then after a period τ, the net spin refocuses, and we see an "echo."

In the spin echo, the applied magnetic field B_0 should have as much homogeneity as possible to eliminate the deviation of Larmor frequency of net spin. On the other hand, if we linearly vary the strength of an external magnetic field, the NMR signal will gradually attenuate, and the diffusion coefficient can be extracted from the relationship between observed NMR signal and gradient strength. It is the central idea of PFG NMR diffusometry and had been developed by Stejskal and Tanner in 1965.[37] Indeed, adding a magnetic field gradient g (G/cm) to a homogeneous B_0, the Larmor frequency ω_{eff} become spatially dependent on the direction of the gradient as shown in Eq. 1.5.[38]

$$\omega_{eff} = \gamma (B_0 + gz) = \omega_0 + \gamma gz \quad (1.5)$$

Where

$$g = \nabla B_0 = \frac{\partial B_z}{\partial x}\mathbf{i} + \frac{\partial B_z}{\partial x}\mathbf{j} + \frac{\partial B_z}{\partial x}\mathbf{k} \quad (1.6)$$

Where **i**, **j**, and **k** are unit vectors.

It is particularly powerful because by just changing the magnetic field in a controlled manner, we can spatially encode the position of spins. Figure 1.6 shows how the spins changed their position when a magnetic field gradient applied to a spin echo pulse sequence. After a 90° rf pulse, the net spin magnetization turns to x-axis. The applied gradient field distorts the net spin and creates a "magnetization helix" with wavelength λ which is calculated in Eq. 1.7

$$\lambda = \frac{2\pi}{\gamma g \delta} \quad (1.7)$$

Where γ is the gyromagnetic ratio of a nucleus; δ is the effective rectangular length of gradient pulse (or the gradient pulse duration), g is maximum gradient strengths

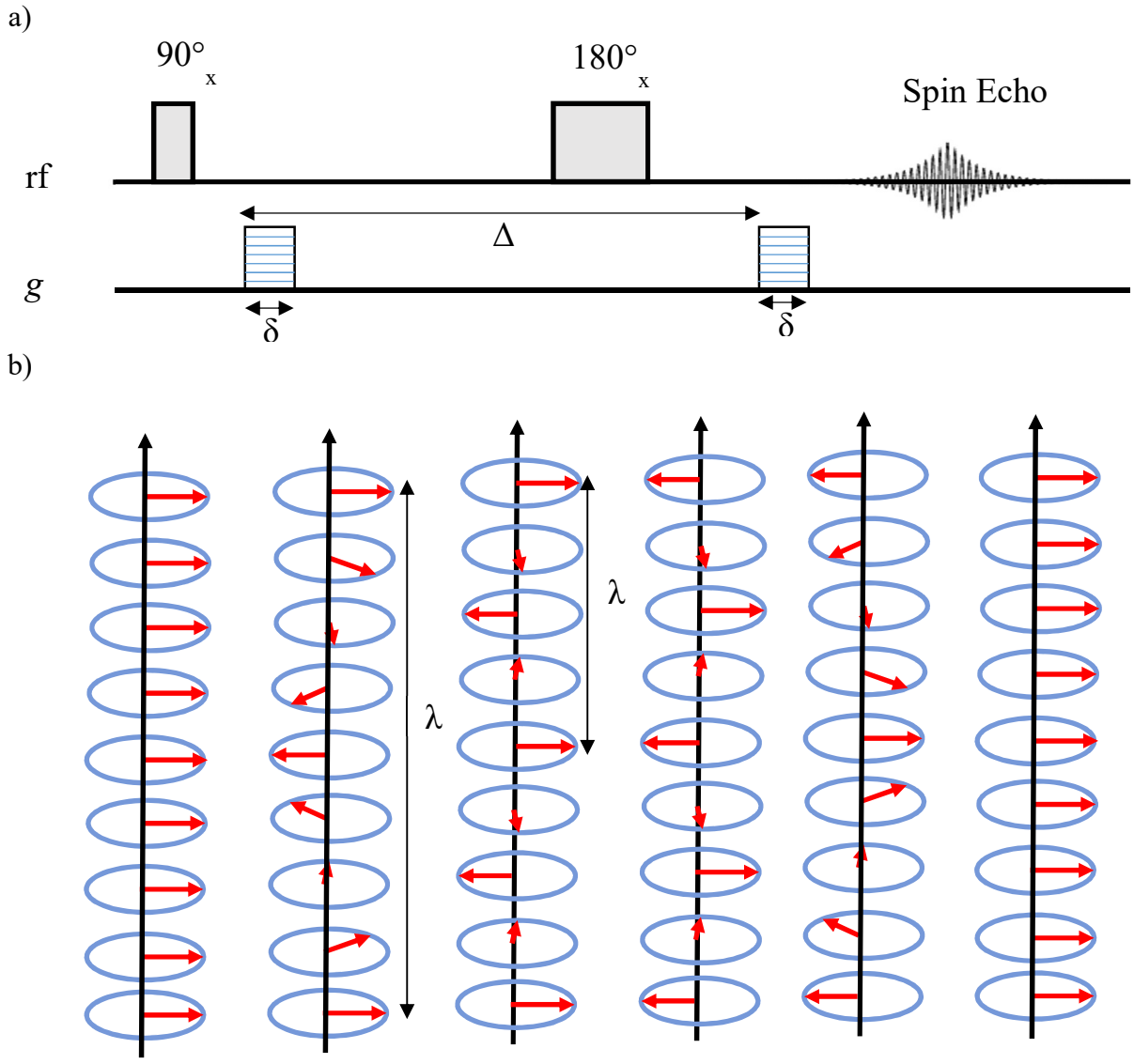

Figure 1.6. An example of the pulse sequence of PFG NMR diffusometry. a) Spin echo rf pulse sequence in the presence of magnetic field gradients b) Illustration of spin assemblage during PFG NMR diffusometry. After a 90° rf pulse, the net spin magnetization turns to x-axis. The applied gradient field distorts the net spin and creates a "magnetization helix" with wavelength λ. A second gradient pulse is applied to turn all the spin to refocus after 180° rf pulse. If there is no diffusion, all the spins will gather in phase, and there will be no NMR signal attenuation. If diffusion happens, there will be some of the spins move out of phase, which eventually results in the attenuation of the NMR signal. Figure reproduced from Callaghan.[39-40]

A second gradient pulse is applied to turn all the spin to refocus after 180° rf pulse. If there is no diffusion, all the spins will gather in phase, and there will be no NMR signal attenuation. If diffusion happens, there will be some of the spins move out of phase, which eventually results in the attenuation of the NMR signal. The relationship between attenuation of signal and diffusion coefficient is given by Stejskal and Tanner in 1965 as shown in Eq. 1.8.[37]

$$I = I_0 e^{-D\gamma^2 g^2 \delta^2 \left(\Delta - \delta/3\right)} = I_0 e^{-Db} \qquad 1.8$$

Where I is the spin-echo signal intensity; I_0 is the signal intensity at zero gradient; γ is the gyromagnetic ratio of a nucleus; δ is the effective rectangular length of gradient pulse, g is maximum gradient strengths; Δ is the duration between the two gradient pulses, and b is the Stejskal- Tanner factor. The self-diffusion coefficient was extracted from the exponential trend line between gradient strength vs. the ratio between the signal at applied gradient (I) and zero gradient (I_0) as shown in Figure 1.7.

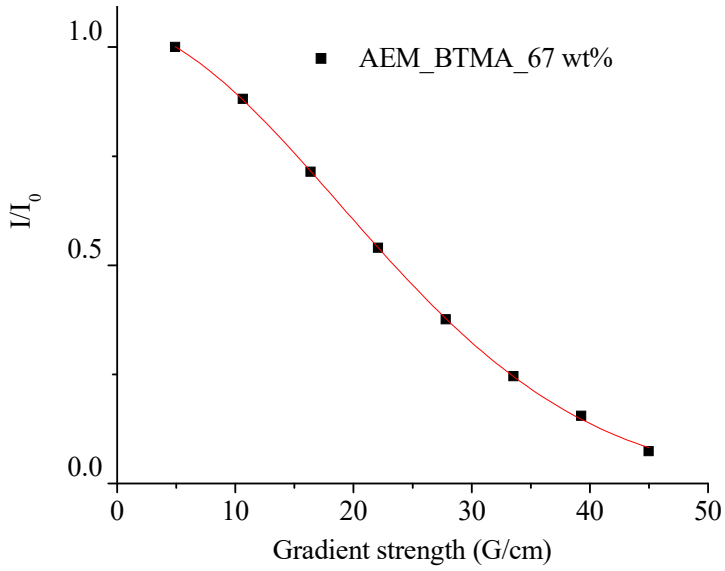

Figure 1.7. The attenuation of signal intensity I/I_0 as a function of gradient strength g during PFG NMR diffusometry and this is called a Stejskal-Tanner curve. This data and fit correspond to water

diffusion inside an anion exchange membrane with 67 wt% water uptake that exhibits a diffusion coefficient $D = 3.4 \times 10^{-10}$ m^2/s ± 5% at 22 °C.

1.4. Restricted diffusion

When water diffuses inside a porous polymer, water will interact with the pathways for transport inside the polymer. The water can reflect from "walls" formed by the hydrophobic polymer and have its motion restricted. We can use the theory of restricted diffusion to explore this behavior in polymer membranes, following and expanding on previous work.[41-42]

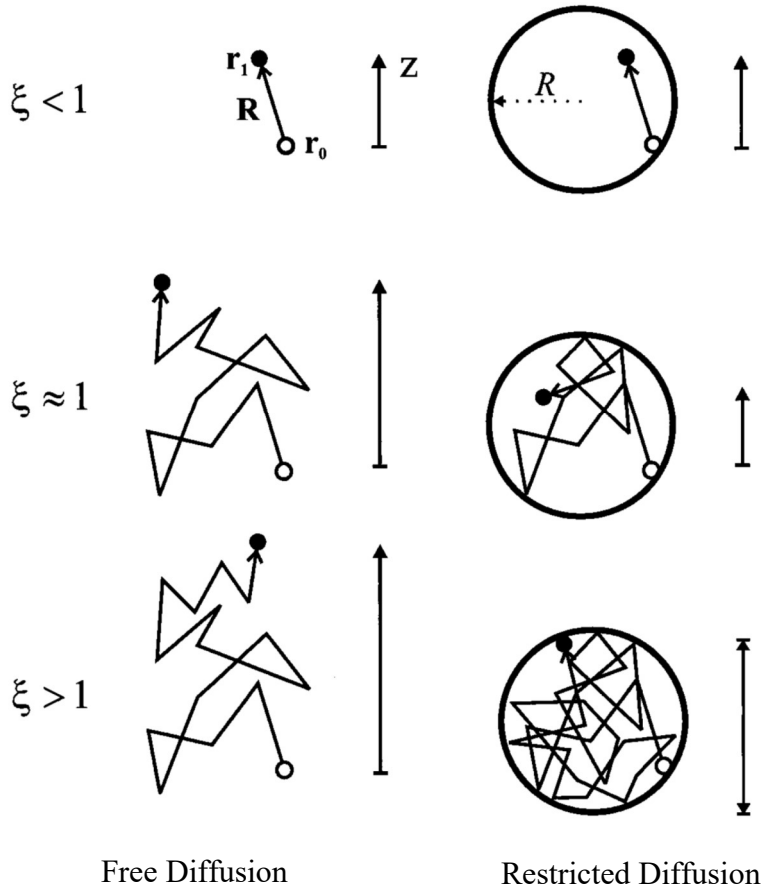

Figure 1.8. Comparison between free diffusion and restricted diffusion. Figure reproduced from Price.[38]

Figure 1.8 displays a particle diffuses in 2 cases, one is free diffusion, or random walk, moving without any restriction and one is restricted diffusion, heading in a limited sphere with radius R. Assume the sphere is reflecting sphere, which the particle cannot move through or relaxed by contact with boundary.

Defined $\xi = \frac{D\Delta}{R^2}$

Where D is diffusion coefficient of the molecule, Δ is diffusion time. The mean-square displacement or the diffusion length of the molecule can be calculated as $< r^2 >^{1/2} = \sqrt{2D\Delta}$

We consider 3 cases of ξ.

Case 1: $\xi < 1$

In this case, the displacement of the molecule is smaller than the radius of the sphere. Therefore, the molecule does not experience any effect of confined geometry. The mean square placement of molecule inside the pore is the same as the mean square placement of molecule in free diffusion and linearly dependent on the Δ.

Case 2: $\xi \sim 1$

In this case, Δ becomes finite, a certain fraction of the particles will feel the effects of the boundary. The mean-square displacement will not linearly depend on the diffusion time. The diffusion coefficient, thus, will contain the information surface-to-volume ratio of confined geometry. Mitra derived the relationship of apparent diffusion and "surface-to-volume ratio of the confining geometry" as shown in Eq. 1.9.[43]

$$\frac{D(t)}{D_0} \approx 1 - \frac{4}{9\sqrt{\pi}}\sqrt{D_0 t}\frac{S}{V} + \varphi\,(\rho, R, T) \qquad 1.9$$

Where D(t) is the diffusion coefficient varied with the diffusion time, D_0 is the bulk diffusion coefficient, t is the diffusion time, S/V is the ratio of surface to volume. $\varphi\ (\rho, R, T)$ is the deviation due to finite surface relaxivity and curvature (R) of the surfaces.

Case 3: $\xi > 1$

At long Δ, all the particles experience the effect of confined environment. Thus the diffusion length and diffusion coefficient no longer depend on Δ. The spin loses its memory about the starting point, and the echo signal attenuation of PFG NMR diffusometry become sensitive to the geometry of the confined environment. If the confined environment is not a single spherical pore, but a set of interconnected spheres, the diffusion coefficient can reveal information about the tortuosity ($\Im$), an important parameter to study interconnected porous networks, as shown in Eq. 1.10.[44] A lower $\Im$ represents a better-connected network.

$$\Im = \frac{D_0}{D_\infty} \qquad 1.10$$

In general, PFG NMR diffusometry is a powerful technique which can give us information about how molecules diffuse in a system. We can use PFG NMR diffusometry to measure diffusion coefficient of water in PEMs. Apart from free diffusion, water diffusion in PEMs is more likely behave as diffuse in a restricted channel. Using this restricted diffusion theory, we can thus gain insight into the influence of morphology on transport in polymer electrolyte membranes,[19-20, 45-46] which helps to improve their conductivity eventually. Ohkubo and his coworker used this theory to explain the behavior of water in Nafion and proposed a 2-steps diffusion attenuation.[42] Our group has previously reported restricted diffusion of water in a polyelectrolyte-fluoropolymer blend membrane caused by micron-scale domain structure.[41] In this study, restricted diffusion of water inside AEMs and CEMs is presented and will be further explained in Chapter 2.

Reference

1. Schäfer, A.; Heywood, J. B.; Weiss, M. A., Future fuel cell and internal combustion engine automobile technologies: A 25-year life cycle and fleet impact assessment. *Energy* **2006,** *31* (12), 2064-2087.
2. Scherer, G. n. G., *Fuel cells I*. Springer: New York ; London, 2008; p xi, 268 p.
3. Maurya, S.; Shin, S. H.; Kim, Y.; Moon, S. H., A review on recent developments of anion exchange membranes for fuel cells and redox flow batteries. *Rsc Advances* **2015,** *5* (47), 37206-37230.
4. Satyapal, S. *Annual Progress Report of DOE Hydrogen and Fuel Cells Program.*; 2015 pp 1-26.
5. Basu, S., *Recent trends in fuel cell science and technology*. Springer ;

Anamaya: New York

New Delhi, 2007; p viii, 375 p.
6. Zhang, H. W.; Chen, D. Z.; Xianze, Y.; Yin, S. B., Anion-Exchange Membranes for Fuel Cells: Synthesis Strategies, Properties and Perspectives. *Fuel Cells* **2015,** *15* (6), 761-780.
7. Elezovic, N. R.; Radmilovic, V. R.; Krstajic, N. V., Platinum nanocatalysts on metal oxide based supports for low temperature fuel cell applications. *Rsc Advances* **2016,** *6* (8), 6788-6801.
8. Hickner, M. A.; Herring, A. M.; Coughlin, E. B., Anion Exchange Membranes: Current Status and Moving Forward. *Journal of Polymer Science Part B-Polymer Physics* **2013,** *51* (24), 1727-1735.
9. Zhu, L.; Pan, J.; Christensen, C. M.; Lin, B. C.; Hickner, M. A., Functionalization of Poly(2,6-dimethyl-1,4-phenylene oxide)s with Hindered Fluorene Side Chains for Anion Exchange Membranes. *Macromolecules* **2016,** *49* (9), 3300-3309.
10. Varcoe, J. R.; Slade, R. C. T.; Wright, G. L.; Chen, Y. L., Steady-state dc and impedance investigations of H-2/O-2 alkaline membrane fuel cells with commercial Pt/C, Ag/C, and Au/C cathodes. *J. Phys. Chem. B* **2006,** *110* (42), 21041-21049.
11. Marino, M. G.; Melchior, J. P.; Wohlfarth, A.; Kreuer, K. D., Hydroxide, halide and water transport in a model anion exchange membrane. *Journal of Membrane Science* **2014,** *464*, 61-71.
12. Pan, J.; Zhu, L.; Han, J.; Hickner, M. A., Mechanically Tough and Chemically Stable Anion Exchange Membranes from Rigid-Flexible Semi-Interpenetrating Networks. *Chemistry of Materials* **2015,** *27* (19), 6689-6698.
13. Agel, E.; Bouet, J.; Fauvarque, J. F., Characterization and use of anionic membranes for alkaline fuel cells. *Journal of Power Sources* **2001,** *101* (2), 267-274.
14. Cheng, J.; He, G.; Zhang, F., A mini-review on anion exchange membranes for fuel cell applications: Stability issue and addressing strategies. *International Journal of Hydrogen Energy* **2015,** *40* (23), 7348-7360.
15. Mamlouk, M.; Scott, K., Effect of anion functional groups on the conductivity and performance of anion exchange polymer membrane fuel cells. *Journal of Power Sources* **2012,** *211*, 140-146.
16. Ous, T.; Arcoumanis, C., Degradation aspects of water formation and transport in Proton Exchange Membrane Fuel Cell: A review. *Journal of Power Sources* **2013,** *240*, 558-582.

17. Lingwood, M. D.; Zhang, Z. Y.; Kidd, B. E.; McCreary, K. B.; Hou, J. B.; Madsen, L. A., Unraveling the local energetics of transport in a polymer ion conductor. *Chemical Communications* **2013,** *49* (39), 4283-4285.
18. Mauritz, K. A.; Moore, R. B., State of understanding of Nafion. *Chemical Reviews* **2004,** *104* (10), 4535-4585.
19. Li, J.; Wilmsmeyer, K. G.; Madsen, L. A., Anisotropic Diffusion and Morphology in Perfluorosulfonate Ionomers Investigated by NMR. *Macromolecules* **2009,** *42* (1), 255-262.
20. Li, J.; Park, J. K.; Moore, R. B.; Madsen, L. A., Linear coupling of alignment with transport in a polymer electrolyte membrane. *Nature Materials* **2011,** *10* (7), 507-511.
21. Owejan, J. P.; Gagliardo, J. J.; Sergi, J. M.; Kandlikar, S. G.; Trabold, T. A., Water management studies in PEM fuel cells, Part I: Fuel cell design and in situ water distributions. *International Journal of Hydrogen Energy* **2009,** *34* (8), 3436-3444.
22. Jiao, K.; Li, X., Water transport in polymer electrolyte membrane fuel cells. *Progress in Energy and Combustion Science* **2011,** *37* (3), 221-291.
23. Peighambardoust, S. J.; Rowshanzamir, S.; Amjadi, M., Review of the proton exchange membranes for fuel cell applications. *International Journal of Hydrogen Energy* **2010,** *35* (17), 9349-9384.
24. Banham, D.; Ye, S.; Pei, K.; Ozaki, J.-i.; Kishimoto, T.; Imashiro, Y., A review of the stability and durability of non-precious metal catalysts for the oxygen reduction reaction in proton exchange membrane fuel cells. *Journal of Power Sources* **2015,** *285*, 334-348.
25. Wang, Y.-J.; Qiao, J.; Baker, R.; Zhang, J., Alkaline polymer electrolyte membranes for fuel cell applications. *Chemical Society Reviews* **2013,** *42* (13), 5768-5787.
26. Hibbs, M. R.; Fujimoto, C. H.; Cornelius, C. J., Synthesis and Characterization of Poly(phenylene)-Based Anion Exchange Membranes for Alkaline Fuel Cells. *Macromolecules* **2009,** *42* (21), 8316-8321.
27. Tang, H.; Peikang, S.; Jiang, S. P.; Wang, F.; Pan, M., A degradation study of Nafion proton exchange membrane of PEM fuel cells. *Journal of Power Sources* **2007,** *170* (1), 85-92.
28. García-Salaberri, P. A.; Sánchez, D. G.; Boillat, P.; Vera, M.; Friedrich, K. A., Hydration and dehydration cycles in polymer electrolyte fuel cells operated with wet anode and dry cathode feed: A neutron imaging and modeling study. *Journal of Power Sources* **2017,** *359*, 634-655.
29. Pinar, F. J.; Rastedt, M.; Pilinski, N.; Wagner, P., Effect of Compression Cycling on Polybenzimidazole-based High-Temperature Polymer Electrolyte Membrane Fuel Cells. *Fuel Cells* **2015,** *15* (1), 140-149.
30. Sigma-Aldrich Nafion® perfluorinated membrane Nafion® 117, thickness 0.007 in. http://www.sigmaaldrich.com/catalog/product/aldrich/274674?lang=en&region=US (accessed Jul 31, 2017).
31. Levitt, M. H., *Spin dynamics : basics of nuclear magnetic resonance*. 2nd ed.; John Wiley & Sons: Chichester, England ; Hoboken, NJ, 2008; p xxv, 714 p., 7 p. of plates.
32. Roberts, J. D., *ABCs of FT-NMR*. University Science Books: Sausalito, Calif., 2000; p xiii, 322 p.
33. Paul, A. L., T.; Vuorinen, V.; Divinski, S. V., *Thermodynamics, diffusion and the Kirkendall effect in solids*. Springer: New York, 2014.
34. A. D. McNaught, A. W., IUPAC. Compendium of Chemical Terminology (the "Gold Book"). In *2nd ed.* [Online] Blackwell Scientific Publications: Oxford 1997. http://goldbook.iupac.org.

35. Nelson, E., *Dynamical theories of Brownian motion*. Princeton University Press: Princeton, N.J.,, 1967; p 142 p.
36. Hahn, E. L., Spin Echoes. *Physical Review* **1950,** *80* (4), 580-594.
37. Stejskal, E. O.; Tanner, J. E., SPIN DIFFUSION MEASUREMENTS: SPIN ECHOES IN THE PRESENCE OF A TIME-DEPENDENT FIELD GRADIENT. *Journal of Chemical Physics* **1965,** *42* (1), 288-292.
38. Price, W. S., Pulsed-field gradient nuclear magnetic resonance as a tool for studying translational diffusion: Part 1. Basic theory. *Concepts in Magnetic Resonance* **1997,** *9* (5), 299-336.
39. Kidd, B. E. Cation and Anion Transport in a Dicationic Imidazolium-Based Plastic Crystal Ion Conductor. Virginia Tech, 2013.
40. Callaghan, P. T., *Translational dynamics and magnetic resonance : principles of pulsed gradient spin echo NMR*. Oxford University Press: Oxford ; New York, 2011; p xvii, 547 p.
41. Hou, J. B.; Li, J.; Mountz, D.; Hull, M.; Madsen, L. A., Correlating morphology, proton conductivity, and water transport in polyelectrolyte-fluoropolymer blend membranes. *Journal of Membrane Science* **2013,** *448*, 292-299.
42. Ohkubo, T.; Kidena, K.; Ohira, A., Determination of a Micron-Scale Restricted Structure in a Perfluorinated Membrane from Time-Dependent Self-Diffusion Measurements. *Macromolecules* **2008,** *41* (22), 8688-8693.
43. Mitra, P. P.; Sen, P. N.; Schwartz, L. M., Short-time behavior of the diffusion coefficient as a geometrical probe of porous media. *Physical Review B* **1993,** *47* (14), 8565-8574.
44. Barrie, P. J., Characterization of porous media using NMR methods. In *Annual Reports on Nmr Spectroscopy, Vol 41*, Webb, G. A., Ed. Elsevier Academic Press Inc: San Diego, 2000; Vol. 41, pp 265-316.
45. Hou, J.; Li, J.; Madsen, L. A., Anisotropy and Transport in Poly(arylene ether sulfone) Hydrophilic−Hydrophobic Block Copolymers. *Macromolecules* **2010,** *43* (1), 347-353.
46. Park, J. K.; Li, J.; Divoux, G. M.; Madsen, L. A.; Moore, R. B., Oriented Morphology and Anisotropic Transport in Uniaxially Stretched Perfluorosulfonate Ionomer Membranes. *Macromolecules* **2011,** *44* (14), 5701-5710.

Chapter 2: Multiscale Tortuous Diffusion in Anion- and Cation-Exchange Membranes: Exploration of Counterions, Water Content, and Polymer Functionality

Lam M. Thieu,[a] *Liang Zhu,*[b] *Andrew G. Korovich,*[a]

Michael A. Hickner, [b] *and Louis A. Madsen,** [a]

[a]Department of Chemistry and Macromolecules Innovation Institute, Virginia Tech, Blacksburg, VA, 24060

[b]Department of Materials Science and Engineering, Pennsylvania State University, State College, PA, 16801

*Louis A. Madsen
Virginia Tech University
Blacksburg, VA 24061
lmadsen@vt.edu

Keywords: fuel cell, anion exchange membrane (AEM), cation exchange membrane (CEM), nuclear magnetic resonance (NMR), diffusion, restricted diffusion, tortuosity

This chapter will soon be submitted for publication in a peer-reviewed journal. Lam Thieu acquired the data and wrote the manuscript. Liang Zhu synthesized the material, and Dr. Michael Hickner and Dr. Louis Madsen provided deep discussions on understanding the data and substantial writing input. Andrew Korovich contributed to the dead end, swelling, and tortuosity model and helped to edit and develop the manuscript.

Abstract

Fundamental understanding of water transport and morphology is critical for improving ion conductivity in polymer electrolyte membranes (PEMs). Herein, we present comprehensive water transport measurements comparing anion-exchange membranes (AEMs) based on ammonium-functionalized poly(phenylene oxide) and cation-exchange membranes (CEMs) based on sulfonated poly(ether sulfone). We investigate the influence of counter ions, alkyl sidechain, and degree of functionalization on water transport in AEMs and CEMs using pulsed-field-gradient (PFG) NMR diffusometry. Water diffusion in both AEMs and CEMs exhibit specific trends as a function of water uptake (wt%), indicating morphological similarities across common chemical structures. Furthermore, restricted diffusion reveals micron-scale heterogeneity of the hydrophilic network in both CEMs and AEMs. We propose a model wherein the hydrophilic network in these membranes has micron-scale distributions of local nm-scale dead ends, leading to changes in tortuosity as a function of water content, counterion type, and polymer structure. We furthermore parse tortuosity into two regimes, corresponding to nm-to-bulk and μm-to-bulk ranges, which reveal the importance of multi-scale morphological structures that influence bulk transport. This study provides new insights into polymer membrane morphology from nm to μm scales with the ultimate goal of controlling polymeric materials for enhanced fuel cells and other separations applications.

2.1. Introduction

As mentioned in Chapter 1, the most popular commercial low-temperature fuel cell (FC) technology currently available utilizes cation exchange membranes (CEMs) such as Nafion®.[1] These membranes employ precious metals such as platinum (Pt) as a catalyst, which is now the main limiter of FC cost. Numerous studies are focused on developing low-Pt-content catalysts by taking advantage of Pt nano-catalysts.[2] V. Stamenkovic and P. Yang et al. have recently developed catalysts with ultra-low platinum content by using a $PtNi_3$ nano-frame.[3] When integrated into a membrane-electrode assembly (MEA), the $PtNi_3$ nano-frame catalyst demonstrated a three-fold increase in the MEA performance of a traditional low loading Pt/C catalyst. While initial results seem promising, more studies about catalysts are needed to reduce the overall price of CEM-based FCs.[4-5]

In addition to catalyst research, anion exchange membranes (AEMs) are an alternative currently being investigated to reduce the cost of FCs. Instead of using CEMs with expensive catalysts, AEMs can employ cheaper metals, such as nickel or silver, and AEMs have received much attention from the scientific community recently.[6-7] Although more than 100 different AEM materials are reported in the literature, high performance examples that can meet all the requirements of practical fuel cells are few. [8-12]

Water transport as a function of water uptake is a crucial topic for both AEM and CEM FCs.[13] While researchers have extensively studied relationships between water uptake, water diffusion, and conductivity in CEMs,[14-17] systematic research on this topic is limited for AEMs. In 2014, Kreuer et al. reported anion and water transport in poly (arylene ether) membranes with directly attached quaternary ammonium (QA) ions.[18] They found that at sufficient hydration ($\lambda \sim$

12), the ionic mobility (diffusion) of AEMs under CO_2-free conditions can be within a factor of 2 of CEMs. Nevertheless, at low water uptake, the diffusion coefficient of hydroxide in AEMs falls more rapidly than the one of hydronium in CEMs, likely due to the less advanced phase-separated morphology in AEMs. Under a CO_2-contaminated environment, the conductivity of AEMs decreased more dramatically because the carbonate form absorbs less water than the OH^- form. Zhao et al. studied the relationship between water uptake and the diffusion coefficient of commercial A201 AEM (Tokuyama, Japan).[19] The measured diffusion coefficient of water in A201 membrane showed the same order of magnitude (10^{-10} m^2/s) as that of Nafion membrane. Cornelius et al. also investigated transport property differences between AEMs and CEMs.[20] While the water self-diffusion coefficient in AEMs (polysulfone with QA) was greater than in CEMs (sulfonated polyphenylenes), the ionic conductivity and pressure-driven water permeability of AEMs were lower than in CEMs. Herring et al. studied restricted diffusion (dependence of the diffusion coefficient of the mobile species on diffusion time) of water in AEMs.[21] They explained that when the diffusion time (Δ) increased, the diffusion of water decreased and reached a constant value when $\Delta \geq 50$ ms. Our group has previously reported multi-scale diffusion phenomena in CEMs due to micron-scale heterogeneity in the porous hydrophilic network phase.[15, 17]

Further extensions to these studies are nevertheless needed to understand the ion and water transport properties (e.g., diffusion and tortuosity) of AEMs, and a clear model of the hydrophilic network in AEMs is still far from complete. Furthermore, the influence of chemical modifications such as alkyl sidechains and degree of functionalization on transport in AEMs and its interplay with morphology has yet to be understood.

Therefore, we have investigated water transport in a series of cationic poly (2,6-dimethyl phenylene oxide) (PPO) AEMs with varying alkyl chain lengths.[22] We compare these random

copolymer AEMs to random copolymer anionic poly(ether sulfone) CEMs and to the benchmark membrane Nafion. For each membrane chemical composition, we use pulsed-field-gradient (PFG) NMR diffusometry to study the relationship between the diffusion coefficient of water (D_{H2O}) as a function of water content (wt. %) and as a function of diffusion time (Δ), the latter of which probes variable diffusion length. We observe common diffusion behaviors in AEMs and CEMs of similar chemical structures and counterion as a function of water content. We further observe that diffusion of water in AEMs and CEMs both decreased with increasing Δ, which reveals a micron-scale structure of restricted pathways for transport inside the polymer matrix. We extract two types of tortuosity values from these measurements (a "microscale tortuosity" and a "nanoscale tortuosity") that we use to understand transport behaviors that depend on morphological structures from nm to μm scales. We combine all of these measurements to investigate trends in transport spanning a range of polymer membrane compositions under different counterion and hydration conditions. Understanding such morphology-molecule-transport behaviors in polymer membranes using NMR diffusometry thus enhances our ability to rationally enhance the performance of AEMs for next generation fuel cells and other molecular separations applications.

2.2. Experimental Section

2.2.1. Materials

There are four series of samples: AEMs, synthesized in the bromide (Br^-) form and then ion exchanged to hydroxide form (OH^-), and CEMs, purchased from Yanjin Polymers Inc in the potassium (K^+) form and then ion exchanged to proton form (H^+). The CEMs are random copolymers of sulfonated poly(ether sulfone) with varying degrees of functionalization (DF) (or

monomers of functionalized) from 20% to 60%. The AEMs are random copolymers of cationic quaternary ammonium poly(2, 6-dimethyl phenylene oxide) (PPO), with a fixed DF of 40%.[22] The AEMs were converted from Br^- to OH^- by immersing in 1M NaOH under N_2 atmosphere for 48 hours. Similarly, the CEMs were converted from K^+ to H^+ by immersing in 1M HCl for 48 hours in ambient atmosphere. The chemical structures and sample's information are shown in Scheme 2.1 and Table 2.1 respectively.

a)

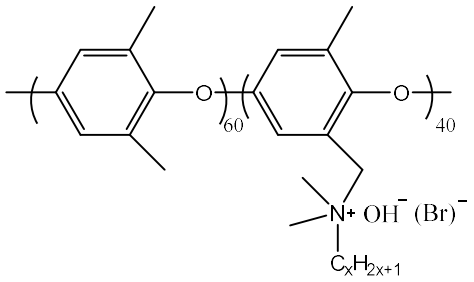

b)

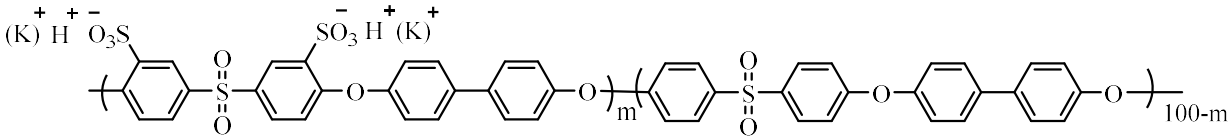

Scheme 2.1. Chemical structure of a) cationic quaternary ammonium poly (2,6-dimethyl phenylene oxide) (PPO) AEM (hydroxide and bromide form) and b) anionic sulfonated polyether sulfone CEM (proton and potassium form).

Table 2.1. Summary of sample information.

Type	Sample	Counter-ion	DF	IEC (meq/g)	Wt. % H_2O (Saturated)	λ
AEM	AEM_BTMAD40 (x = 1) (BTMA)	OH^-	40	2.67	130.0	27.0
	AEM_C6D40 (x=6) (C6)			2.25	66.0	16.0
	AEM_C10D40 (x=10) (C10)			2.00	46.0	13.0
	AEM_C16D40 (x=16) (C16)			1.71	54.0	18.0
	AEM_BTMAD40 (x=1) (BTMA)	Br^-		2.28	33.0	8.0
	AEM_C6D40 (x=6) (C6)			1.97	21.0	5.8
	AEM_C10D40 (x=10) (C10)			1.77	19.0	5.9
	AEM_C16D40 (x=16) (C16)			1.54	22.0	7.9
CEM	CEM_D60 (m=60) (D60)	H^+	60	2.42	96.0	22.0
	CEM_D50 (m=50) (D50)		50	2.08	65.0	17.0
	CEM_D40 (m=40) (D40)		40	1.72	42.0	14.0
	CEM_D30 (m=30) (D30)		30	1.34	29.0	12.0
	CEM_D20 (m=20) (D20)		20	0.93	68.0	41.0
	CEM_D60 (m=60) (D60)	K^+	60	2.22	55.0	14.0
	CEM_D50 (m=50) (D50)		50	1.93	30.0	8.6
	CEM_D40 (m=40) (D40)		40	1.62	27.0	9.2
	CEM_D30 (m=30) (D30)		30	1.27	19.0	8.4
	CEM_D20 (m=20) (D20)		20	0.89	41.0	26.0

The IEC was calculated from the equivalent weight of the polymer and compared with the IEC from reference.[22] Each sample name is expressed as follows. The type of membrane is followed by the number of the alkyl chain, then the degree of functionalization is followed by the counterion type. For example, AEM_C16D40_OH (C16_OH in short) refers to an anion exchange membrane with the percent of functionalized monomers (or degree of functionalization) equal to 40%, and attached to a 16-carbon alkyl sidechain with a hydroxide counterion. CEM_D20_K (D20_K in short) refers to a cation exchange membrane with a degree of functionalization equal to 20%, no alkyl sidechain attachment and with a potassium counterion. In total, there are 8 AEMs: BTMA,

C6, C10, and C16 with each in OH^- and Br^- form, and 10 CEMs: D20, D30, D40, D50, and D60 with each in H^+ and K^+ form.

2.2.2. NMR Sample Preparation

Membranes were cut into 4 mm × 4 mm pieces, stacked together (6-14 layers) to enhance NMR signal and wrapped with PTFE tape. Each sample was soaked in distilled deionized water for at least 48 hours to obtain saturated water uptake, then quickly blotted with Kimwipes to remove surface water and wrapped in LDPE plastic food wrap. Finally, each sample was sealed inside a custom PTFE cell with low dead (air) volume,[15-17] designed for an 8 mm coil, to eliminate water content changes during NMR analysis. An equilibration time of 30 minutes after sealing was used for membrane samples. To control the water content, the sample was removed from the cell and left on the balance for water to evaporate until it achieved the desired mass ($mass_{wet}$). After finishing the NMR experiments, each sample was dried in a vacuum oven at 60 °C overnight to obtain the dry mass ($mass_{dry}$). Water content was determined using the following equation:

$$wt.\,\%\,H_2O = \frac{mass_{wet} - mass_{dry}}{Mass_{dry}} \times 100 \qquad 2.1$$

, where $mass_{wet}$ and $mass_{dry}$ stand for the mass of wet and dry membranes, respectively.

Water content was converted to lambda (λ) (number of H_2O per QA anionic or cation site) by the following equation:

$$\lambda = \frac{wt.\,\%\,H_2O \times 10}{IEC \times M_{water}} \qquad 2.2$$

In which, $wt.\,\%\,H_2O$ is the water content, IEC represents ion-exchange capacity (meq/g), M_{water} is the molecular weight of water in g/mol.

2.2.3. Pulsed-Field-Gradient (PFG) NMR Diffusometry

^1H_2O self-diffusion measurements were performed using the pulsed-gradient stimulated echo (PGSTE) NMR pulse sequence at 22 °C on a Bruker Avance III 9.4T wide-bore spectrometer corresponding to a ^1H frequency of 400.13 MHz. A magnetic resonance imaging probe ("Bruker Micro5") equipped with triple-axis gradients and an 8 mm ^1H radio frequency coil was used. The NMR signal attenuation due to diffusion is described by the Stejskal-Tanner equation:[23]

$$I = I_0 e^{-Dy^2 g^2 \delta^2 \left(\Delta - \delta/3\right)} = I_0 e^{-Db} \qquad 2.3$$

where I is the spin-echo signal intensity at a given gradient strength g (maximum values used in the range 20 – 300 G/cm), I_0 is the signal intensity at zero gradient, and γ is the gyromagnetic ratio of ^1H nucleus (26752 rad $s^{-1}G^{-1}$). δ (= 2 ms) is the effective rectangular length of gradient pulse (actual half sinusoid gradient pulse length was δ = 3.14 ms), Δ (= 8 ms to 1 s) is the diffusion time or duration between the two gradient pulses, and b is the Stejskal-Tanner factor that encompasses all pre-set PGSTE parameters. The spin relaxation times T_1 and T_2 varied from 250 ms to 1500 ms and 8 ms to 150 ms, respectively. The PGSTE sequence was used with 90° pulse lengths = 6 μs and each diffusion experiment used eight gradient steps and 16 scans per step. D is the self-diffusion coefficient of the mobile species extracted by fitting the signal attenuation (I/I_0) curve as a function of g with Equation 2.3.

2.3. Result and Discussion

2.3.1. Determine D_{H2O} inside AEMs and CEMs

Figure 2.1a shows the 1D pulse-acquire ^1H-NMR spectrum of water in AEM_BTMA_OH at 67 wt. % H_2O (water content). As we can see, there is a broad peak and a narrow single peak corresponding to polymer and water NMR signals. The water peak in AEM_BTMA_OH included both OH^- and

H_2O species, but the exchange process between these species occurs too fast for NMR to distinguish separate signals. The obtained D_{H2O} is thus an average of these species, and this is similar for acidic species and water in CEMs. In the PFG NMR diffusometry experiment, the broad polymer peak disappeared due to relaxation time weighting from the PGSTE experiment, and we obtained only the narrow peak as illustrated in Figure 2.1b. We applied PFG NMR diffusometry through an 8-step attenuation process to determine D_{H2O} (Figure 2.1c). Figure 2.1d displays the signal attenuation curves for measurement of D_{H2O} in AEM_BTMA_OH 67 wt. %, AEM_C6_OH 30 wt. % and CEM_D50_K 30 wt. % with values shown on the plot.

a)

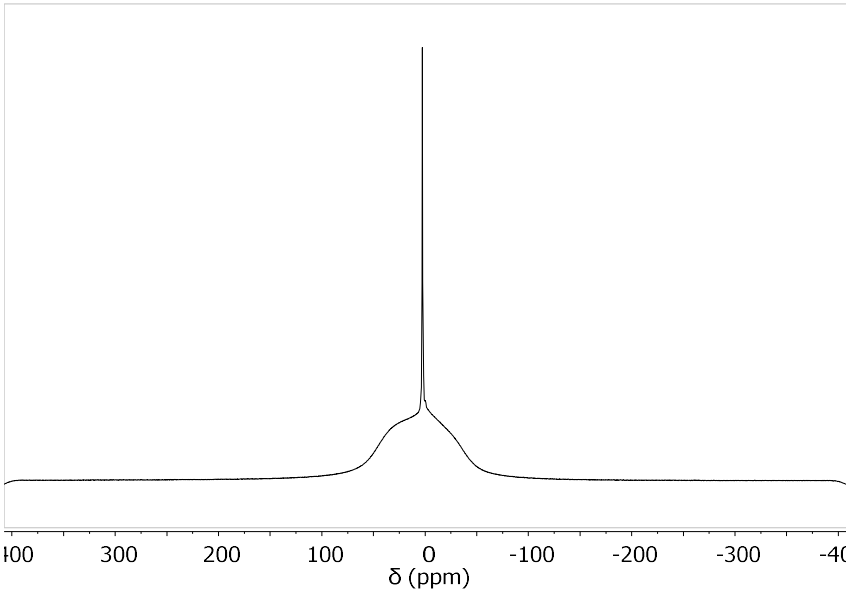

b)

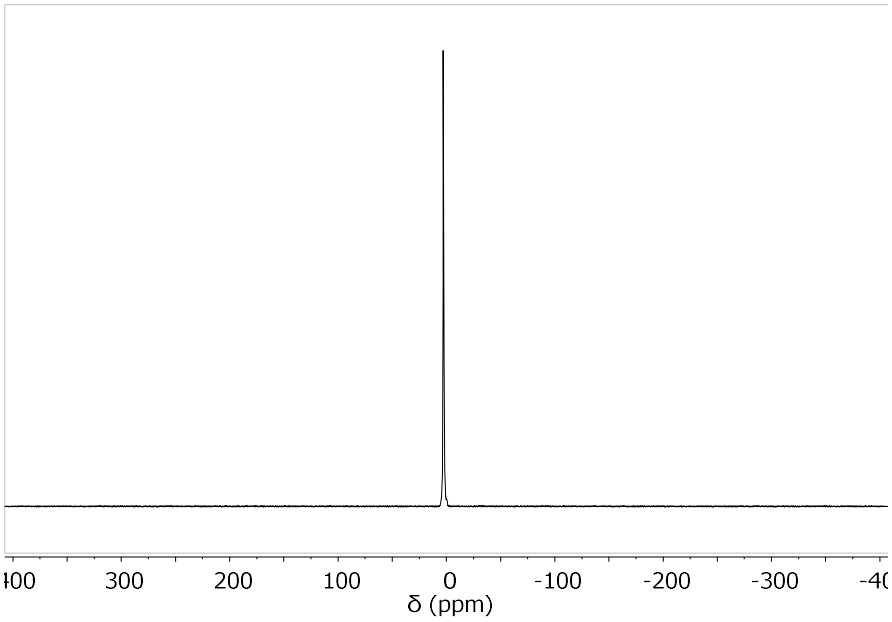

c)

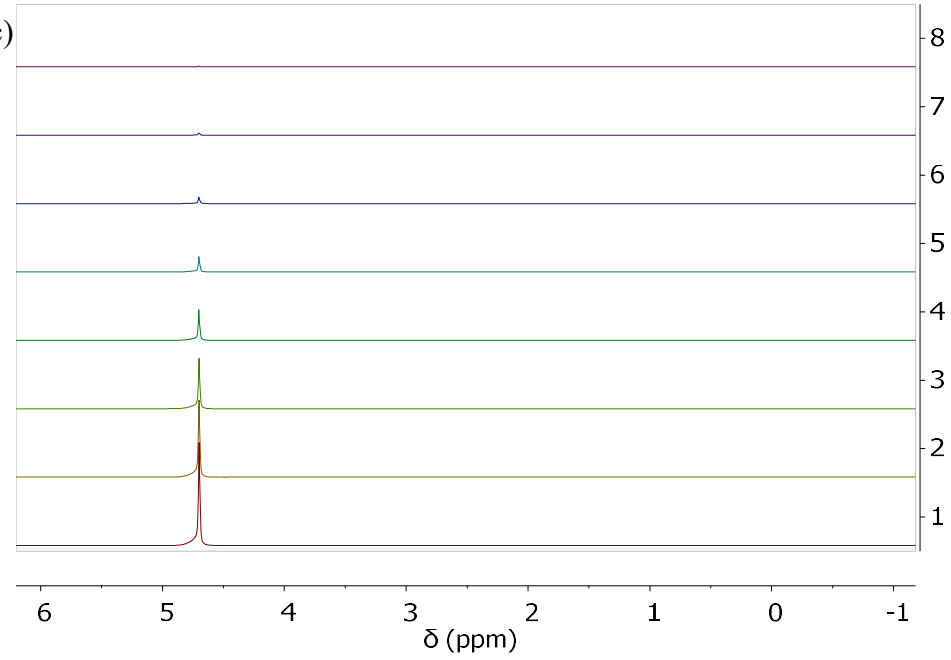

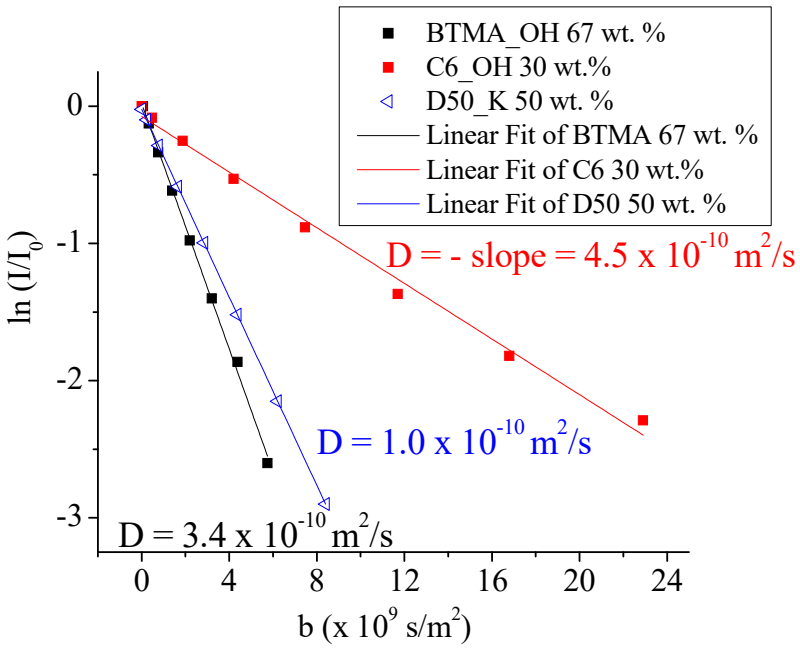

Figure 2.1 a) 1D pulse-acquire ^{1}H-NMR of AEM_BTMA_OH 67 wt. % at 22°C. The broad peak and the narrow peak correspond to polymer and water. b) The first slice of the PFG NMR diffusometry spectrum of AEM_BTMA_OH 67 wt. %. The broad peak disappears, and only the narrow (water) peak remains. c) Individual slices (spectra) from an 8-step PFG NMR diffusometry experiment on the representative sample AEM_BTMA_OH at 67 wt. % water uptake. d) Normalized NMR signal intensity ln (I/I_0) vs. Stejskal-Tanner factor b of AEM_BTMA_OH 67 wt. %, AEM_C6_OH 30 wt. % and CEM_D50_K 50 wt. %. The slope of the fit line is the D_{H2O} . Errors in diffusion coefficients are ±5%.

2.3.2. D_{H2O} vs. water content

Figure 2.2 shows the relationship between D_{H2O} and water content (wt. % H_2O) for AEMs and CEMs. The filled squares and triangles represent AEM_OH (samples with OH^- counter-ion) and AEM_Br (samples with Br^- counter-ion) respectively, while the red and black empty shapes represent CEM_H (samples with H^+ counter-ion) and CEM_K (samples with K^+ counter-ion),

respectively. Nafion in proton form was used as a reference sample. Figure 2.2a compares the water diffusion of AEM_OH and CEM_H (see also Figure 2.4a). Among AEMs, AEM_BTMA_OH exhibited the highest saturated water content, leading to a higher D_{H2O}, followed by AEM_C6_OH, AEM_C10_OH, and AEM_C16_OH. When alkyl sidechain length increased, the water content of these membranes decreased because hydrophobicity limits water absorption into the AEMs. As shown in Figure 2.2a, all AEM_OHs appear to follow a master curve with wt. % uptake (black dashed line to guide the eye). We note here that dependencies of transport on water uptake in terms of wt. % should correlate more strongly with morphological structure, while dependencies on uptake in terms of λ (water molecules per ionic group, see next section) should reflect local molecular-scale changes. Thus, our smooth wt. % dependence indicates morphological similarity among these membranes. In other words, altering alkyl sidechain length does not substantially influence the morphology of AEMs. Similarly, all of the CEM_Hs followed a master curve (red dashed line) and showed faster diffusion by a factor of ≈ 1.5 relative to the AEM_OHs, which is slightly smaller than the ratio of the proton and hydroxide diffusion coefficient in free aqueous solution.[24] In free solution, the local water-water and water-ion molecular interactions are the main determining factors for water diffusion. On the other hand, in a PEM both the local interactions and the morphology of the membrane influences diffusion of water. This leads to the differing ratio of the proton and hydroxide diffusion coefficients in PEMs as compared to aqueous solution. Nafion showed the highest D_{H2O} compared to CEM_H and AEM_OH, although it absorbed less water, presumably due to its strongly interconnected nanophase-separated hydrophilic channel structure.[14-16]

Figure 2.2b compares the diffusion of water in CEM_K and CEM_H. Increasing the degree of functionalization of CEMs leads to an increase in water uptake of the membranes, resulting in faster diffusion. CEM_H, in general, showed somewhat slower diffusion than CEM_K. Furthermore, all CEM_Hs followed a similar trend while CEM_Ks did not, indicating some morphological difference between CEM_Ks and CEM_Hs. As shown in Figure 2.2c, AEM_Br showed a fairly similar diffusion behavior compared to AEM_OH, but if we look closely at the expanded region (Figure 2.2d), the diffusion behavior of AEM_C6_OH and AEM_C10_OH follows the same curve while AEM_Br and AEM_C16_OH deviate from this the trend. It appears that the long hydrophobic alkyl spacer of AEM_C16 restricts the mobility of water, likely due to a change in self-organized morphology, which results in slower water diffusion. In addition, changing the counterion type leads to faster water diffusion in AEM_Br, which is most pronounced in BTMA_Br. This might be attributed to the electronegativity difference of the counterions (Br^- vs. OH^-), which likely modifies the local hydrophilic phase morphology.

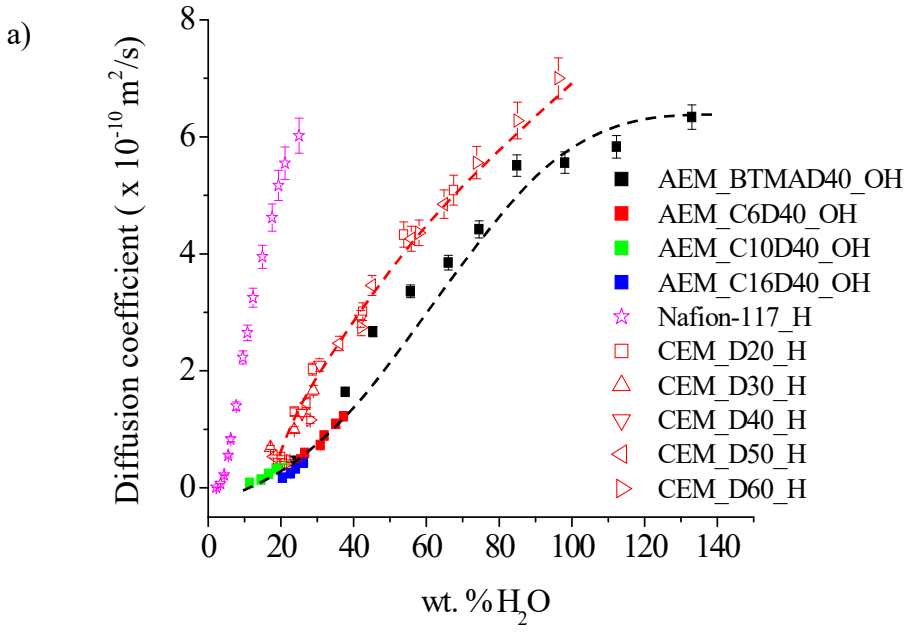

b)

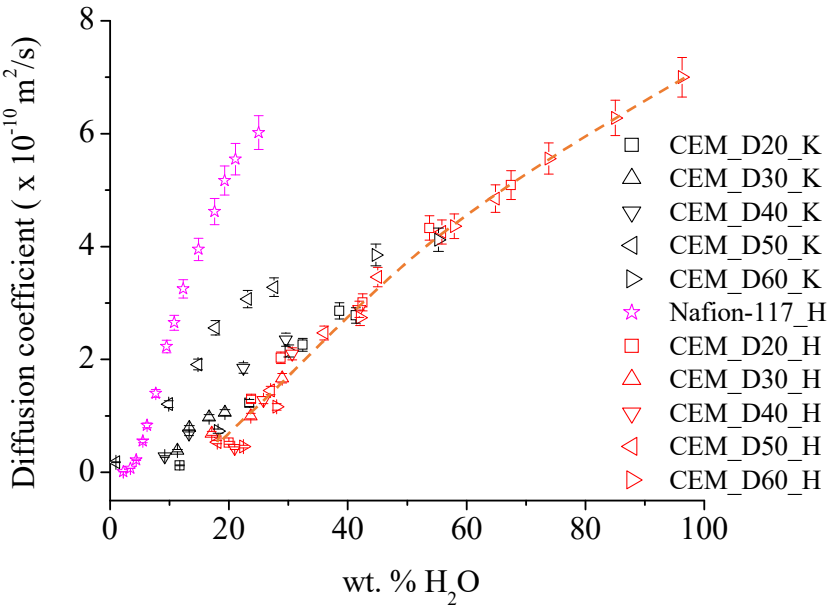
Diffusion coefficient (x 10^{-10} m^2/s)
wt. % H_2O
CEM_D20_K
CEM_D30_K
CEM_D40_K
CEM_D50_K
CEM_D60_K
Nafion-117_H
CEM_D20_H
CEM_D30_H
CEM_D40_H
CEM_D50_H
CEM_D60_H

c)

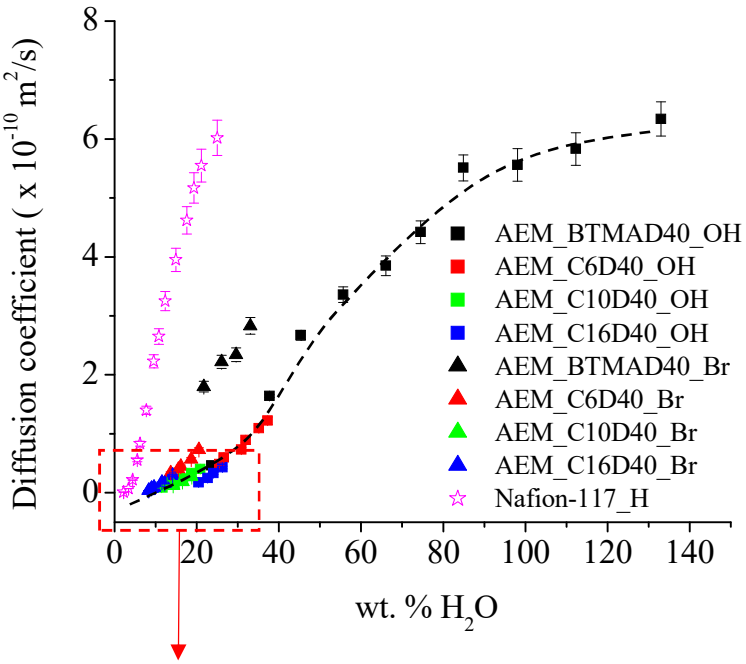
Diffusion coefficient (x 10^{-10} m^2/s)
wt. % H_2O
AEM_BTMAD40_OH
AEM_C6D40_OH
AEM_C10D40_OH
AEM_C16D40_OH
AEM_BTMAD40_Br
AEM_C6D40_Br
AEM_C10D40_Br
AEM_C16D40_Br
Nafion-117_H

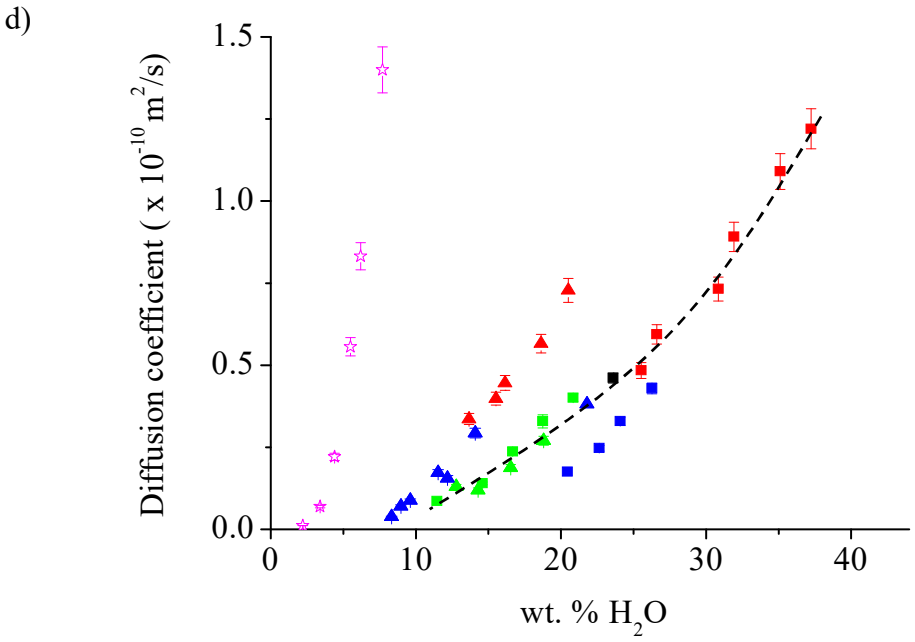

Figure 2.2. D_{H2O} in AEMs and CEMs obtained by ^{1}H NMR diffusometry as a function of water content (wt %). a) AEM_OH (samples with OH^- counter-ion) vs. CEM_H (samples with H^+ counter-ion). b) CEM_H vs. CEM_K. c) AEM_Br vs. AEM_OH. d) Expanded view of Figure 2.2c. We used Nafion as a reference sample. AEM_OH and CEM_H membranes appear to follow master curves, shown by the dashed lines (black and red, guides to the eye). CEM_H materials show faster diffusion than AEM_OH. CEM_K and CEM_H show different diffusion behavior indicating a counterion effect on morphology. The diffusion behavior of AEM_C6_OH and AEM_C10_OH follows the same curve while the AEM_Br and AEM_C16_OH deviate from this the trend. On the contrary, changing the counterion type leads to faster water diffusion in AEM_Br, which is most pronounced in BTMA_Br. Error bars for D_{H2O} measurement range from ±5% for high water content and ±10% for low water content. All measurements performed at 22°C.

2.3.3. D_{H2O} vs. λ (water – ion mole ratio)

Figure 2.3 plots D_{H2O} as a function of λ. The λ or water–ion mole ratio is the number of H_2O per QA anionic or sulfonated cationic site, and it closely relates to IEC. λ can also refer to molar concentration of polymer ionic groups C_M, as shown in Equation 2.4.

$$\lambda = \frac{1000}{C_M M_{water}} \qquad 2.4$$

To understand the internal molecular environment of AEMs and CEMs, we measured the D_{H2O} in trifluoromethane sulfonic acid (HOTf), p-Toluene sulfonic acid (TsOH), and tetramethylammonium hydroxide (TMAOH). Our group and others have previously used HOTf to study the internal environment of perfluorosulfonate ionomers (PFSIs).[25-26] Here, we use HOTf, TsOH, and TMAOH as solution-state analogs to the local molecular environments in Nafion, sulfonated polyether sulfone CEM and quaternary ammonium PPO AEM, respectively. At high λ (low ion concentration), D_{H2O} in TMAOH approach those in TsOH (λ = 39) as displayed in Figure 2.3a. As λ decreases, D_{H2O} of TMAOH falls more rapidly than TsOH and is about a half of D_{H2O} of TsOH at λ = 7.5. In general, the HOTf solutions gives the fastest water diffusion, followed by TsOH, and TMAOH. The remarkable water diffusion in HOTf is ascribed to its super acidity (pKa ~ -14),[27] which contributes to superior water transport in Nafion.[26]

Figure 2.3b compares the water diffusion behavior of AEM_OH and CEM_H. Similar to water diffusion in HOTf, TsOH, and TMAOH, Nafion also shows the fastest diffusion, followed by slower diffusion in CEMs and then slowest in AEMs. In contrast to water diffusion as a function of wt. % H_2O (Figure 2.2), water diffusion of AEMs and CEMs as a function of λ do not follow a similar trend curves. CEM_D20_H has the lowest IEC among all of these membranes, which led to the lowest diffusion curve in Figure 2.3b. This lowest curve followed by CEM_D30_H,

CEM_D40_H, CEM_D50_H, and CEM_D60_H (only CEM_D20 and CEM_D60 shown in the Figure 2.3b) (See Figure 2.4b for all samples). AEMs also show the similar trend: C16 had the lowest IEC which led to the lowest diffusion. The D_{H2O} inside AEM_OHs increases with IEC, as evident for C6, C10, and BTMA. It is important to note that the relationship between D_{H2O} and λ is a combination of local molecular interactions, IEC, and to some extent morphology. Therefore, although IEC of CEM_D60_H is lower than that of AEM_BTMA_OH, its diffusion curve is still higher than AEM_BTMA_OH due to its faster local water transport and possible morphology differences (see Figures 2.8-2.10 below and associated tortuosity discussion).

Figure 2.3c shows the diffusion of CEM_K and CEM_H. Generally, the CEM_K curves overlap the CEM_H curves because of their similar IECs and local water diffusion environment. Clearly, when degree of functionalization increases, maximum water absorption increases leading to faster diffusion. Water diffusion in CEM_K exceeds the CEM_H marginally because of its low IEC relative to CEM_H.

Figure 2.3d compares the diffusion vs. λ of AEM_Br and AEM_OH. Similar to CEMs, AEMs do not fall onto the similar trend curves as in Figure 2.2c. This arises due to the variation of local molecular environments for water transport, modulated by IEC, by alkyl sidechain length and by counterion type. Further systematic study will be needed to understand the details of these subtle molecular-scale differences.

a)

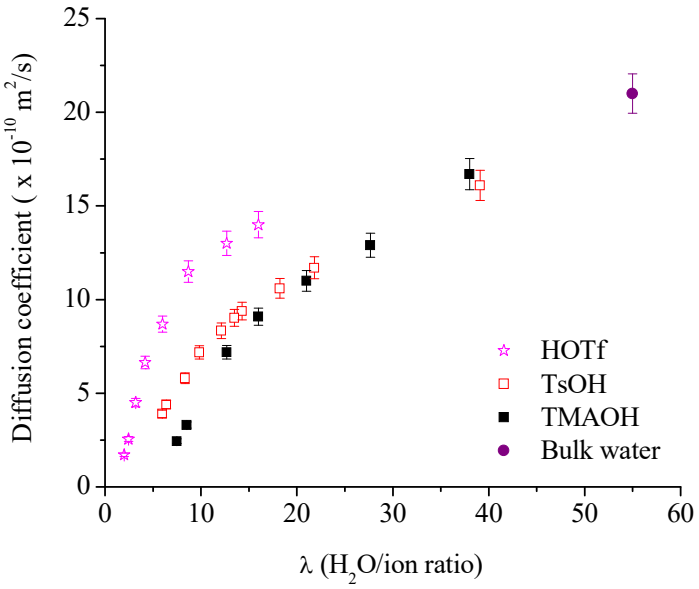
Diffusion coefficient (x 10^{-10} m^2/s)
λ (H$_2$O/ion ratio)
HOTf
TsOH
TMAOH
Bulk water

b)

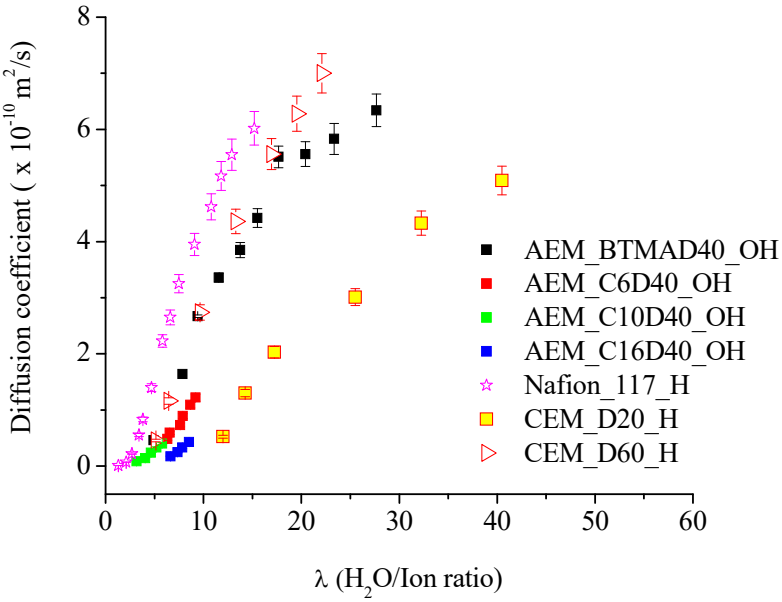
Diffusion coefficient (x 10^{-10} m^2/s)
λ (H$_2$O/Ion ratio)
AEM_BTMAD40_OH
AEM_C6D40_OH
AEM_C10D40_OH
AEM_C16D40_OH
Nafion_117_H
CEM_D20_H
CEM_D60_H

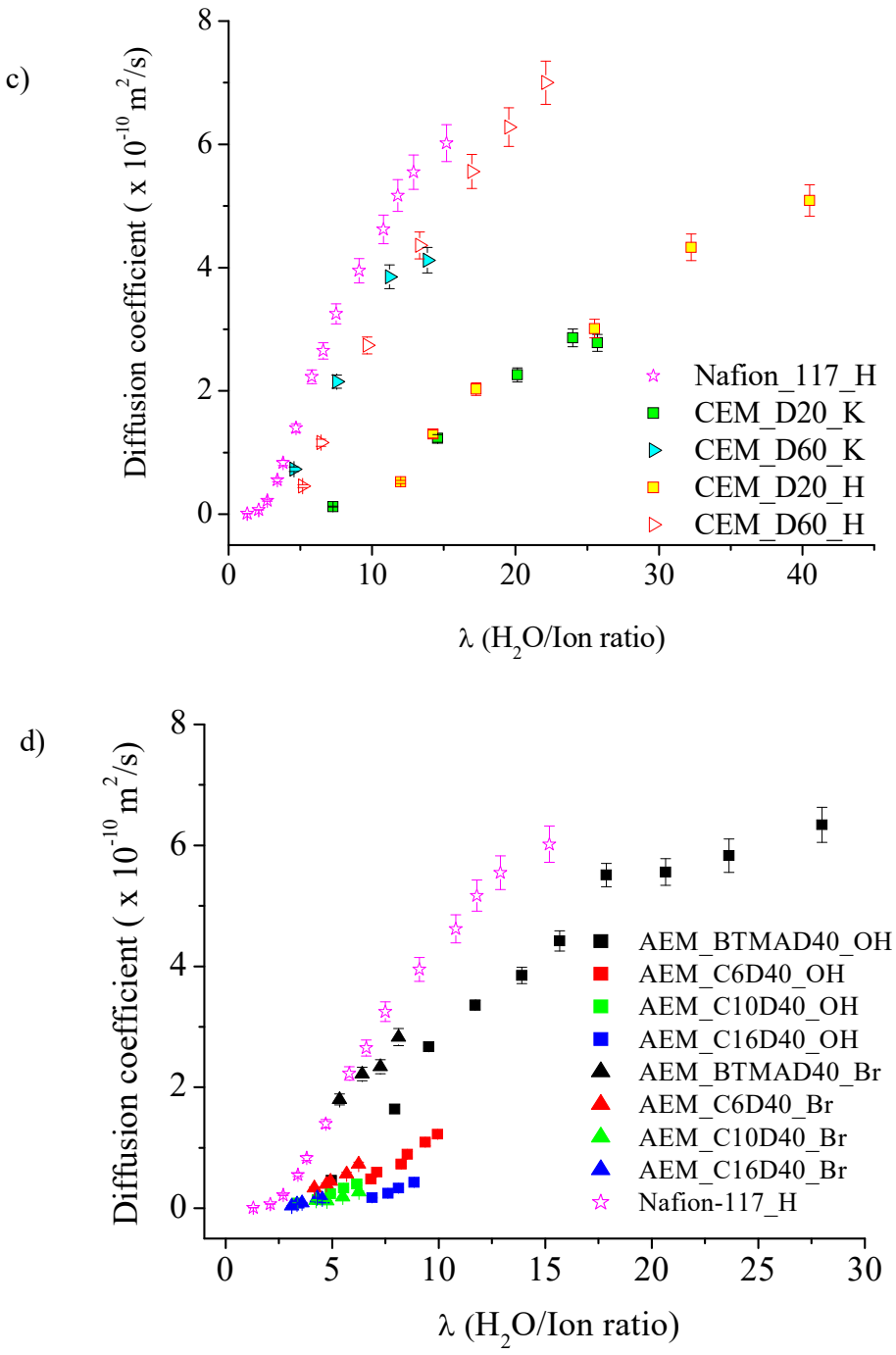

Figure 2.3. D_{H2O} in AEMs and CEMs obtained by ^{1}H NMR diffusometry as a function water-ion mole ratio λ. a) HOTf, TsOH and TMAOH as free liquid solutions. b) AEM_OH vs. CEM_H. c) CEM_H vs. CEM_K. d) AEM_Br vs. AEM_OH. We used Nafion as a reference sample. At high λ (low ion concentration), D_{H2O} for TMAOH approaches that of TsOH (λ = 39). As λ decreases,

D_{H2O} for TMAOH falls more rapidly than for TsOH and is about a half D_{H2O} for TsOH at $\lambda = 7.5$. AEM_OHs and CEM_Hs do not follow similar trend curves as in Figure 2.2. The relationship between D_{H2O} and λ is indicative largely of variations due to local ion-water interactions. Error bars for D_{H2O} measurement are ±5% for high water content and ±10% for low water content. All measurements performed at 22°C.

In short, the differences of diffusion behavior observed as a function of water wt. % and of λ can expose general pictures of morphology and local molecular (ion–water) as summarized in Figure 2.4. Regarding wt. % dependencies, AEM_OH and CEM_H appeared to follow the same curve, indicating similarity of morphology. Varying counter ion type does change morphology in both AEMs and CEMs, although the shift is stronger for CEMs. Water diffusion in these CEMs, in general, is faster than AEMs. Water diffusion in CEM_K is faster than CEM_H, and water diffusion in AEM_Br is faster than AEM_OH. Regarding λ dependencies, molecular interactions between counterions, polymer-fixed ionic sites, alkyl sidechains, and water drive substantial variations in bulk water transport. For AEMs, counterion type and alkyl sidechain length drives substantial changes in local transport, while in CEMs we vary degree of functionalization, which produces a much stronger variation in local transport than counterion type change. In the next section, we further explore morphology and local molecular effects through the use of "restricted diffusion" measurements (D_{H2O} vs. diffusion encoding time Δ) combined with concepts of tortuosity.

.

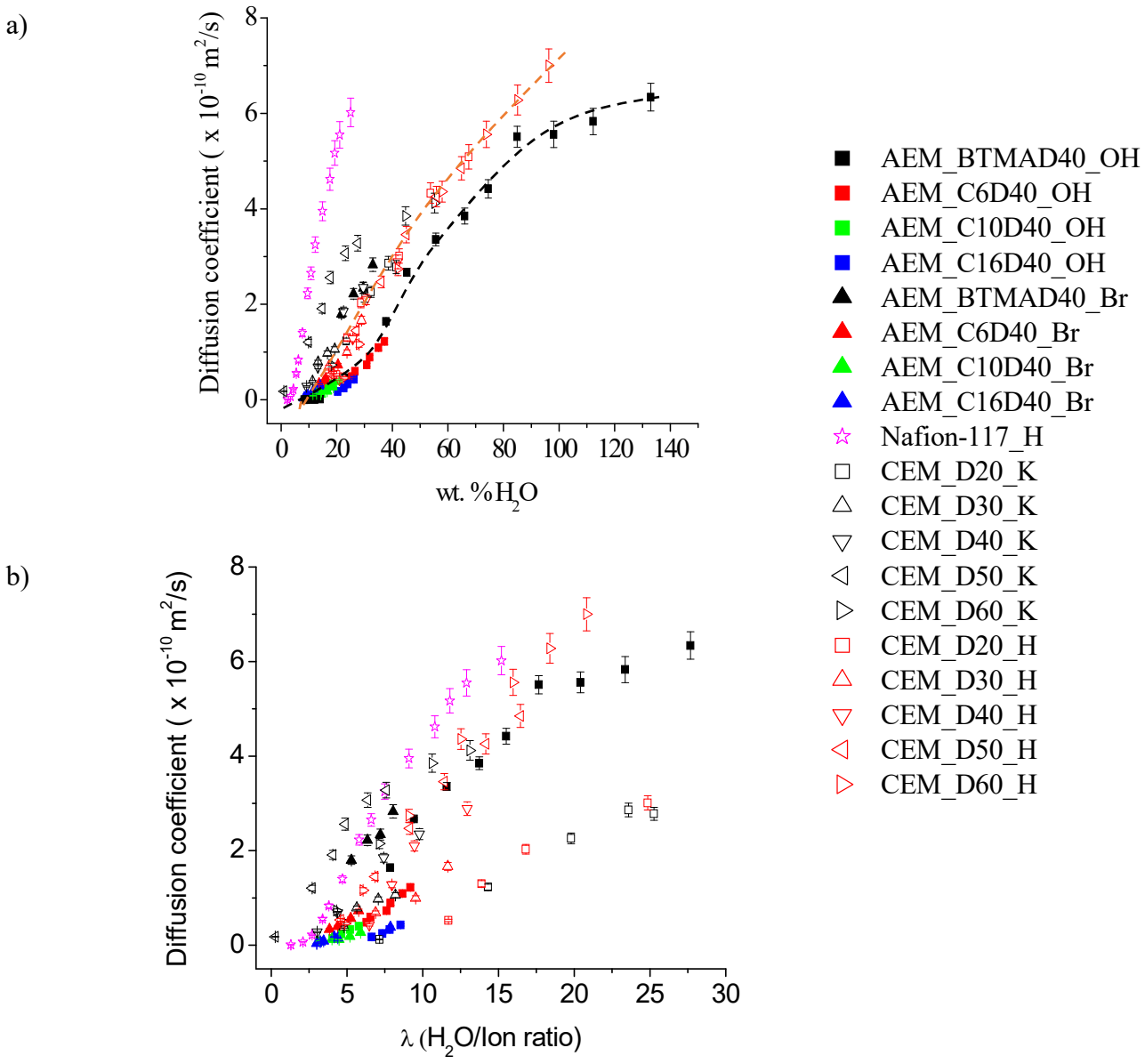

Figure 2.4. The diffusion coefficient of H_2O inside AEMs and CEMs obtained by ^1H NMR diffusometry at 22 °C as a function a) water wt. % b) water-ion mole ratio (λ). Nafion was used as a reference sample. The dotted lines are simply guides to the eye. The difference of diffusion behavior between λ and water content can show us the picture of general morphology and local

morphology (ion – water interaction). Error bars for diffusion coefficient measurement are ≤ ±5% for high water content and ≤ ±10% for low water content sample.

2.3.4. Restricted water diffusion

Figure 2.5 illustrates the relationship between D_{H2O} and the *diffusion time* Δ of water inside AEM_OH and CEM_H at saturated (top) and similar (bottom) water uptake. Both CEM_H and AEM_OH display a similar basic trend: when diffusion time Δ increases, water molecules interact with heterogeneous restrictions (such as domain boundaries or walls) leading to a decrease in D_{H2O}, usually to an asymptotic value. Δ can also be easily converted to *diffusion length* l_D by Equation 2.5.

$$l_D = < r^2 >^{1/2} = \sqrt{2D\Delta} \qquad 2.5$$

where $<r^2>^{1/2}$ is the root-mean-square displacement that molecules undergo during the NMR diffusometry experiment. Among AEM_OHs, BTMA_OH absorbs the most water, resulting in the highest $D_{H2O} = 7.4 \times 10^{-10}$ m^2/s at Δ = 8 ms and corresponding to diffusion length l_D = 2.4 μm. D_{H2O} then decreased to 4.8×10^{-10} m^2/s at Δ = 512 ms or l_D = 15.6 μm. AEM_C6_OH, AEM_C10_OH, and AEM_C16_OH exhibit the same phenomenon. Compared to AEMs, D_{H2O} for CEMs has a weaker dependence on Δ demonstrating that CEM_H has a less restricted micron-scale hydrophilic transport network (morphology) than AEM_OH. We note that D_{H2O} in extruded Nafion 117 is independent of Δ, with Δ ranging from 4 ms to 1000 ms.[28-29]

At saturated water uptake, D_{H2O} in AEM_OH and CEM_H varies widely because diffusion depends strongly on how much water the membrane can absorb. Nevertheless, if we fix the water content for all membranes near 20 wt. %, D_{H2O} for all AEM_OHs fall on the same trend curve, where for all membranes D_{H2O} decreased from approximately 7×10^{-11} m^2/s at Δ = 8 ms (or l_D

= 0.8 μm) to 2 × 10^{-11} m^2/s at diffusion time of Δ = 512 ms (or l_D = 2.7 μm). On the other hand, D_{H2O} curves for different CEM_H membranes do not collapse as neatly onto one trend curve.

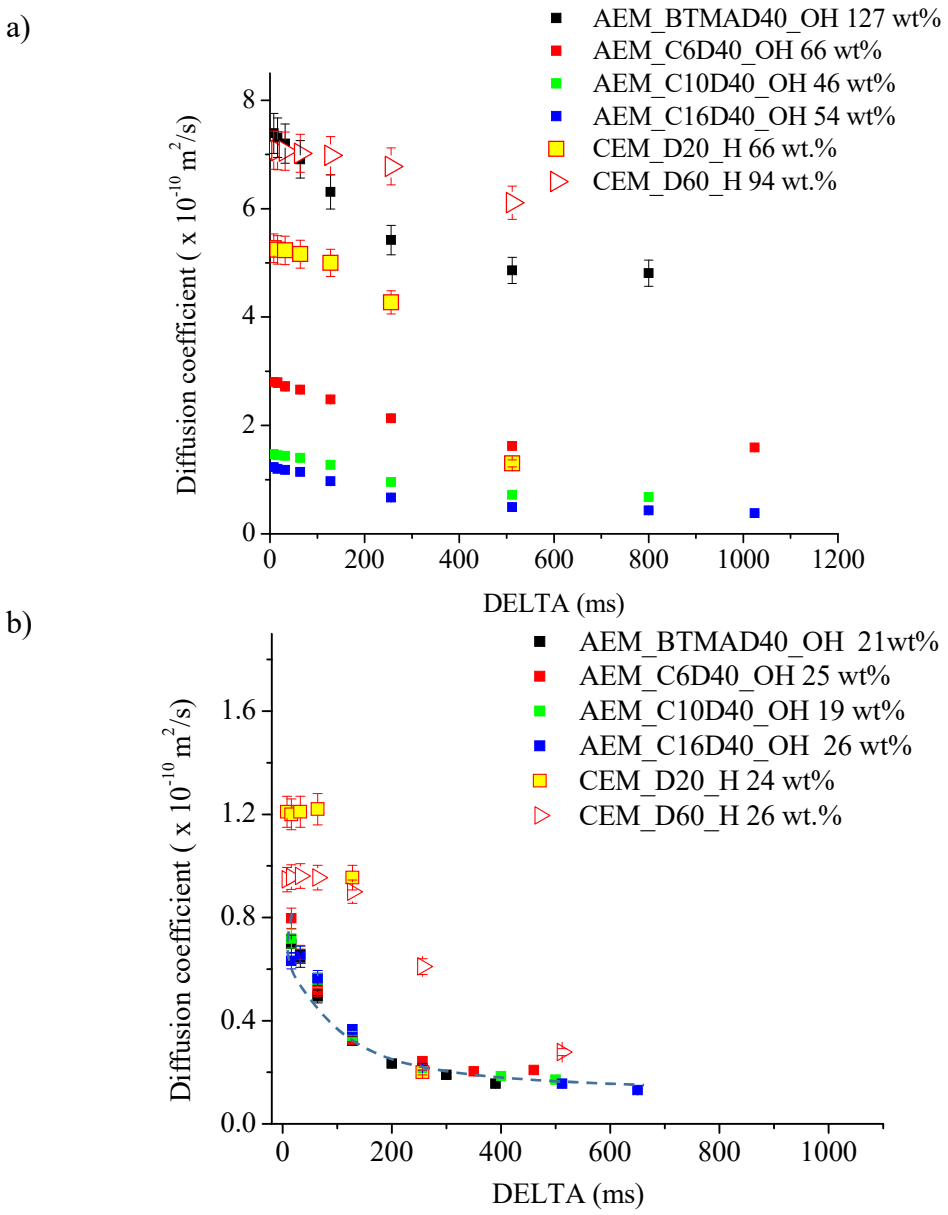

Figure 2.5. Water diffusion D_{H2O} vs. diffusion time Δ for AEM_OH and CEM_H at a) saturated and b) similar water uptake. The dotted lines are guides to the eye. At saturated water uptake, all membranes show restricted diffusion, although CEMs show decreasing D_{H2O} at longer Δ values as compared to AEMs. At similar water content, AEMs closely follow a trend curve while CEMs do

not. Error bars for D_{H2O} are ±5% at short Δ and ±10% for long Δ. All measurements performed at 22°C.

Figure 2.6 shows how counterion type influences morphology in AEMs by comparing the diffusion behavior of water inside AEM_OH and AEM_Br at both saturated and similar water uptakes. D_{H2O} for both AEM_OH and AEM_Br decreases when Δ increases. AEM_Br absorbs less water than AEM_OH, and therefore D_{H2O} for water-saturated AEM_Br is much smaller than for AEM_OH. However, at similar water content (wt. %), all AEM_OH and AEM_Br membranes fall onto the same trend curve. We note the exception of BTMA-Br, which presumably has a substantially different morphology due to the combination of the Br^- counterion and the absence of an alkyl sidechain. This behavior confirms what we observe in the above section, where changing the counterion has relatively little influence on the morphology of AEMs.

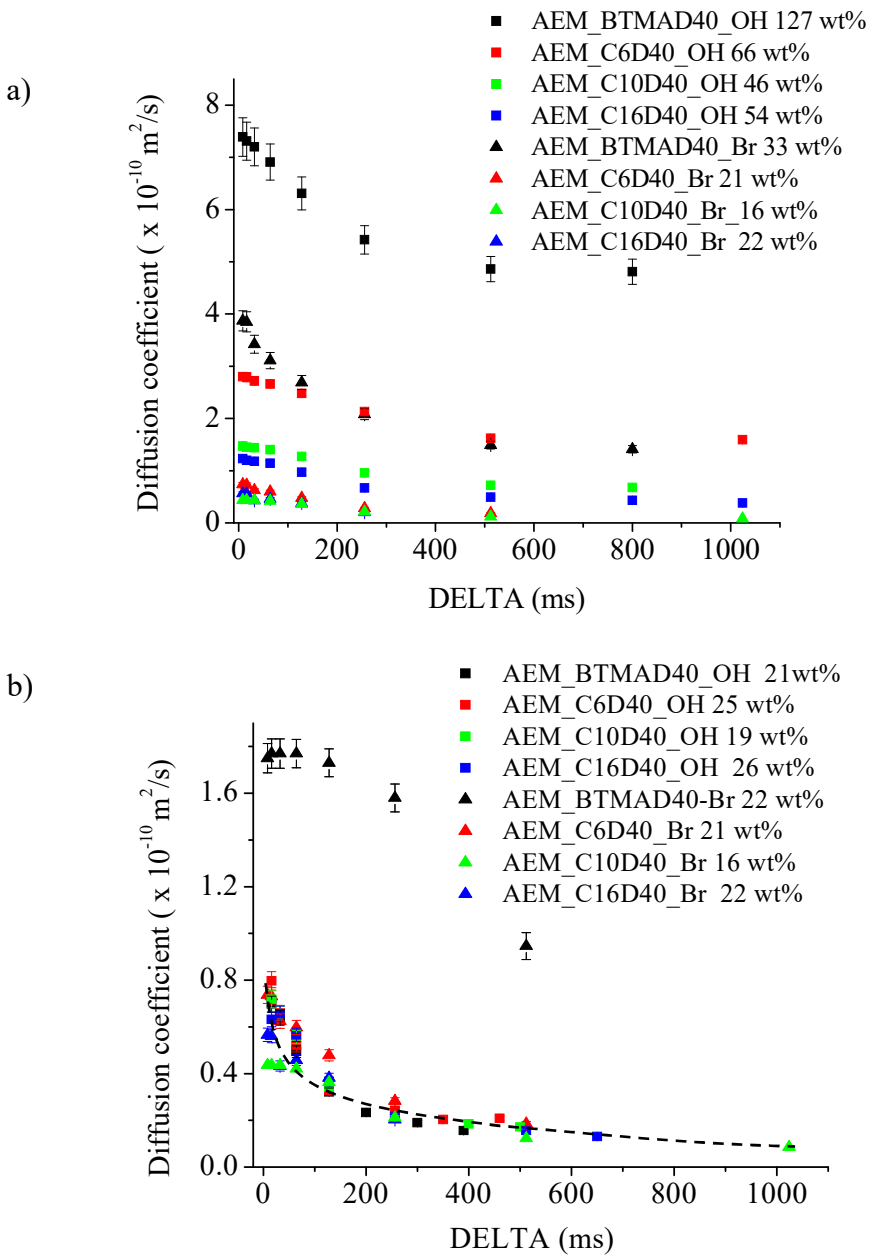

Figure 2.6. Water diffusion D_{H2O} vs. diffusion time Δ for AEM_OH and AEM_Br at a) saturated and b) similar water uptake. The dotted lines are guides to the eye. At similar water content, AEMs fall onto the same trend curve indicating similar morphology on the scale of the diffusion length of the measurements (0.5 – 20 μm). Changing counterion type does not significantly influence the morphology of AEMs. Error bars for D_{H2O} are ±5% at short Δ and ±10% for long Δ. All measurements performed at 22°C.

In contrast to AEMs, changing counterion type does makes a more pronounced difference in CEM morphology, as shown in Figure 2.7. CEM_K absorbed less water than CEM_H and therefore D_{H2O} for CEM_K was smaller than for CEM_H. However, D_{H2O} for CEM_K showed a shallower dependence and less severe drop at longer Δ as compared to CEM_H. This effect was more pronounced at similar water content (Figure 2.7b). These water diffusion behaviors demonstrate that the morphology of CEMs significantly changes with counterion type.

In summary, AEMs show more strongly restricted diffusion on μm length scales than CEMs, while CEM_Hs show more restricted diffusion than CEM_Ks. Changing counterion creates significantly more change to the diffusion in CEMs as compared to AEMs. These restricted diffusion behaviors in AEMs and CEMs indicate μm-scale heterogeneity of the hydrophilic transport network, which will be further explored in the following section.

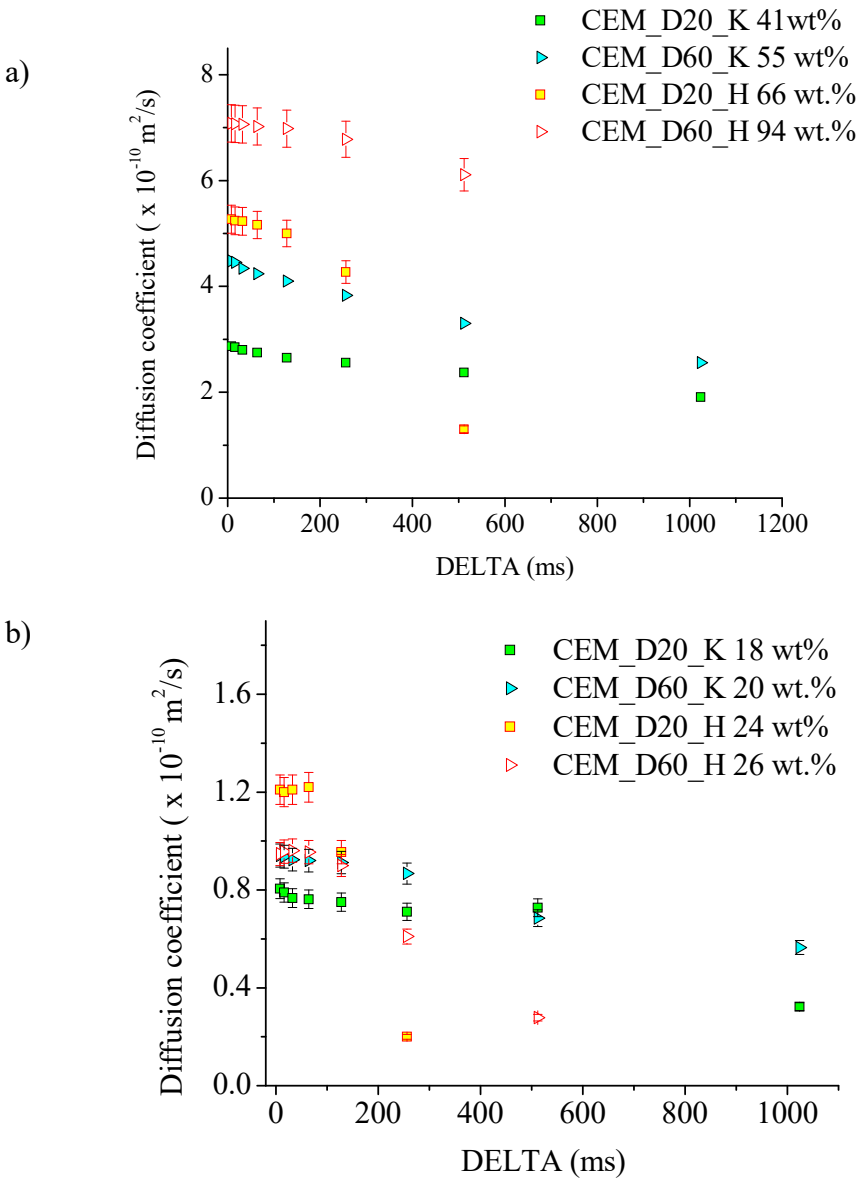

Figure 2. 7. Water diffusion D_{H2O} vs. diffusion time Δ for CEM_H and CEM_K at a) saturated and b) similar water uptake. Changing counterion type influences the water transport and thus the µm-scale morphology of CEMs. Error bars for D_{H2O} are ±5% at short Δ and ±10% for long Δ. All measurements performed at 22°C.

2.3.5. Multi-scale tortuosity in membranes

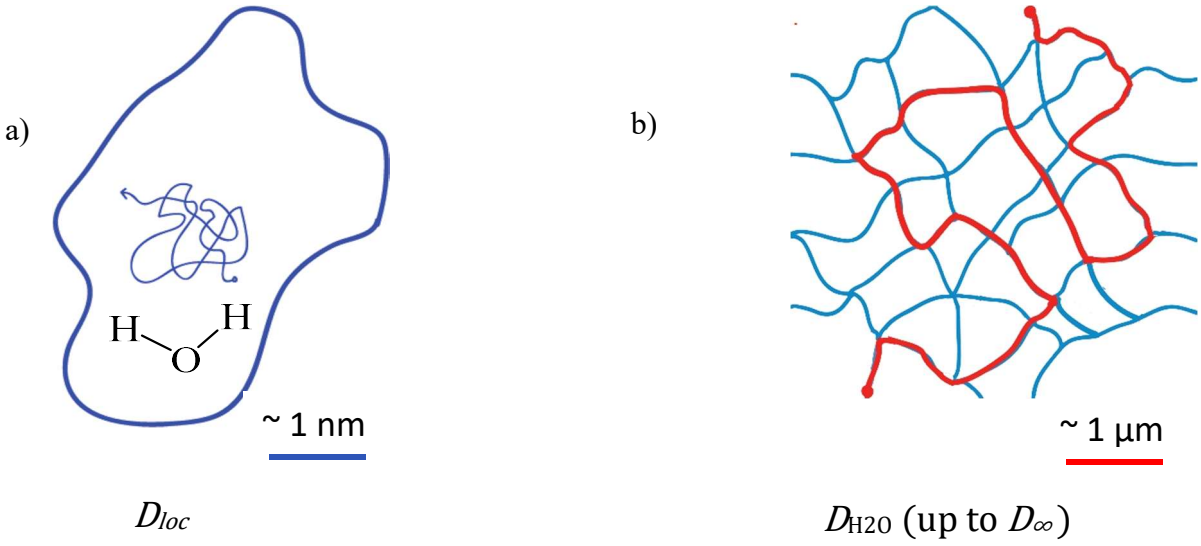

Figure 2.8. Illustration of tortuosity of the hydrophilic channel of PEMs a) Water molecule travels inside a cavity at short diffusion time b) Tortuous length of water molecule at long diffusion time

Consider a water molecule diffusing in a confined pore with radius R.[30] Assume the pore is a reflecting pore, in which the particle cannot move through the wall or boundary. If the mean-square displacement, or square of the diffusion length $l_D^2 = D\Delta$ is less than R^2, which is equivalent to the displacement of the molecule being smaller than the radius of the pore, then the molecule does not experience the confined pore. In this regime, the molecule experiences what we define as the local diffusion coefficient (D_{loc}), which is independent of Δ and is depicted in Figure 2.8a. If $l_D^2 = D\Delta \sim R^2$, a fraction of the molecules will feel the effects of the pore boundary, leading to a decrease in observed D. If $l_D^2 = D\Delta >> R^2$, the obtained diffusion coefficient will directly reflect the tortuosity ($\mathfrak{I}$) of the network.[31] This model has seen wide application in a wide array of porous media (usually hard materials),[32] and recently this has found use in porous polymeric systems such as PEMs,[15] in which boundaries may not be hard walls, but instead can represent µm-scale domain heterogeneities.

Tortuosity is an important parameter to study interconnected porous networks in which a lower $\mathfrak{I}$ represents a more fully connected network allowing more direct paths for diffusion. $\mathfrak{I}$, as averaged over all length scales above the local molecular scale, can be defined in terms of diffusion coefficients as shown in Equation 2.6.[33]

$$\mathfrak{I} = \frac{D_{loc}}{D_{\infty}} \qquad 2.6$$

In this study, D_{loc} represents the local diffusion coefficient that water molecules would experience within each nm-scale hydrophilic pore, as depicted in Figure 2.8a. While nanoconfinement effects may influence this intra-pore diffusion,[25] in this study we make the simplfying approximation that D_{loc} is the diffusion coefficient of a bulk liquid solution with a similar ion concentration and ion types to those in the membrane interior (Figure 2.3a and Table 2.3). D_{∞} is the diffusion coefficient of probe molecule at infinite diffusion time Δ (or length l_D), as depicted in Figure 2.8b. $\mathfrak{I}$ necessarily is ≥ 1, where $\mathfrak{I} = 1$ is the tortuosity of an isotropic pure liquid.

PFG NMR diffusometry has been widely applied to characterize the tortuosity of conventional macroporous materials by measuring D for probe molecules inside pores as a function of Δ.[32, 34] For example, if we use water as the molecular probe and measure the D_{H2O} in 10 ms, the diffusion length l_D = 7 μm ($< r^2 >^{1/2} = \sqrt{2D\Delta} = \sqrt{2 \times 2.3 \times 10^{-9} \times 10^{-2}} = 6.8 \times 10^{-6}$ m) or about the pore size of a conventional macroporous material such as a rock. For polymer membranes, PFG NMR diffusometry thus can extract observed D_{H2O} over a range of length scales spanning approximately 0.1 to 100 μm, and including D_{∞} the bulk D_{H2O} through the whole membrane.

We can consider AEMs and CEMs a porous material, in which the hydrophobic part of the polymer forms a structural matrix and the hydrophilic cavities form a porous network.[15] Since the

hydrophilic cavities in PEMs are on the order of nanometers, we observe a long time (ms) and μm-scale average using PFG NMR diffusometry. However, we can vary Δ to measure different D_{H2O} values that encompass any μm-scale heterogeneities in the membrane.[35,15] If we minimize Δ, (with a lower limit of a few ms) we measure what we define as D_0. D_0 represents D_{H2O} averaged over the smallest length accessible by NMR diffusometry, usually ~ 0.1 μm. Thus, we can subdivide the network tortuosity into two separate parameters:

$$\mathfrak{I}_{L-B} = \frac{D_{loc}}{D_\infty} \tag{2.7}$$

$$\mathfrak{I}_{M-B} = \frac{D_0}{D_\infty} \tag{2.8}$$

To summarize, $\mathfrak{I}_{L-B}$ is the "nano-to-bulk tortuosity" that arises from structures that range all the way from local molecular scales (nm) to bulk; $\mathfrak{I}_{M-B}$ is the "micron-to-bulk tortuosity" that arises from morphological heterogeneities that range from micrometer scale to bulk.

To be more specific to this study, D_{loc} is the D_{H2O} obtained in free liquid solutions as shown in Figure 2.3a and Table 2.3, where for AEMs we use TMAOH as the local diffusion standard, for CEMs we use TsOH, and for Nafion we use HOTf. For each solution used to determine D_{loc} for a given membrane composition and hydration, we adjust the solution lambda to mimic lambda inside the membrane. D_∞ is the D_{H2O} measured at the largest Δ accessible due to the limitations in water ^{1}H T_1 relaxation time.[15] By employing the above analysis, $\mathfrak{I}_{L-B}$ and $\mathfrak{I}_{M-B}$ provide quantitatively separable insights into how molecular transport is affected by morphological structures over widely different length scales in polymer membranes. Further refinements to this model are underway, focusing especially on the aspects of intra-pore nanoconfinement and local molecular environment.[25, 36-37]

Table 2.2. Tortuosity of AEMs and CEMs

	Water wt%	IEC (meq/g)	λ	D_0 (x 10^{-10} m^2/s)	D_∞ (x 10^{-10} m^2/s)	D_{loc} (x 10^{-10} m^2/s)	$\Im_{M-B}$	$\Im_{L-B}$
BTMA-OH	130.0	2.67	27.0	7.30	4.80	13.0	1.5	2.7
BTMA-OH	21.0	2.67	4.40	0.70	0.15	1.2	4.7	8.0
C6-OH	66.0	2.25	16.0	2.80	1.60	9.1	1.8	5.7
C6-OH	25.0	2.25	6.20	0.80	0.21	2.0	3.8	9.6
C10-OH	46.0	2.00	13.0	1.50	0.68	7.2	2.1	11.0
C10-OH	19.0	2.00	5.30	0.72	0.17	1.5	4.2	8.8
C16-OH	54.0	1.71	18.0	1.20	0.38	9.2	3.2	24.0
C16-OH	26.0	1.71	8.40	0.63	0.13	3.3	4.8	25.0
D20_H	68.0	0.93	41.0	5.20	1.30	16.0	4.0	12.0
D20_H	24.0	0.93	14.0	1.20	0.20	9.4	6.0	47.0
D30_H	29.0	1.34	12.0	1.70	0.34	8.3	5.0	25.0
D30_H	24.0	1.34	10.0	1.10	0.43	7.2	2.7	17.0
D40_H	42.0	1.72	14.0	3.10	0.61	9.0	5.1	15.0
D40_H	26.0	1.72	8.40	1.60	0.21	5.8	7.8	28.0
D50_H	65.0	2.08	17.0	5.01	2.60	11.0	1.9	4.1
D50_H	24.0	2.08	6.40	1.04	0.46	4.4	2.3	9.6
D60_H	96.0	2.42	22.0	7.07	6.10	12.0	1.2	1.9
D60_H	26.0	2.42	6.0	0.96	0.28	3.9	3.5	14.0

Table 2.3. Diffusion coefficient of water in Triflic acid (HOTf), p-Toluene sulfonic acid (TsOH), and Tetramethylammonium hydroxide (TMAOH)

	λ	D (x 10^{-10})		λ	D (x 10^{-10})		λ	D (x 10^{-10})
Triflic acid (HOTf)	16.0	14.0	p-Toluene sulfonic acid (TsOH)	39.0	16.0	Tetramethyl ammonium hydroxide (TMAOH)	38.0	17.0
	13.0	13.0		22.0	12.0		28.0	13.0
	8.7	12.0		18.0	11.0		21.0	11.0
	6.0	8.7		14.0	9.4		16.0	9.1
	4.2	6.6		13.0	9.0		13.0	7.2
				12.0	8.3		8.5	3.3
				10.0	7.2		7.5	2.5
				39.0	16.0			
				22.0	12.0			
				18.0	11.0			

Figure 2.9 shows $\Im_{L-B}$ and $\Im_{M-B}$ for both CEMs and AEMs as a function of water content. Additionally, all information concerning tortuosity and measured D_{H2O} for membranes and free

solutions is summarized in Tables 2.2 and 2.3. As shown in Figure 2.9a, $\mathfrak{I}_{L-B}$ strongly depends on water uptake, where the membranes show between a factor of 1.5 and 5 drop in $\mathfrak{I}_{L-B}$ with increasing water content. AEM_BTMA_OH absorbed the most water, resulting in a low $\mathfrak{I}_{L-B}$ at saturated water content, although at a similar (~ 20 wt. %) water content, AEMs with alkyl sidechains from BTMA to C10 had the similar $\mathfrak{I}_{L-B}$, implying the similarity of hydrophilic network. However, C16 displays a significant higher $\mathfrak{I}_{L-B}$ than other AEMs because the long hydrophobic alkyl spacer of AEM_C16 restricts the mobility of water, resulting to a poorer interconnected network. Among CEMs, D20 showed the highest $\mathfrak{I}_{L-B}$, assumedly related to its low degree of (hydrophilic) functionalization that provides for poor phase-separation and thus weak hydrophilic cavity connectivity relative to D60. In general, the tortuosity of CEMs is higher than AEMs (except AEM_C16), indicating that overall the water transport *morphology* in CEMs is worse than AEMs. Since in general CEMs have faster overall diffusion than AEMs (Figure 2.2a) at equivalent water wt. %, this emphasizes that the *local molecular effects* contributing to bulk diffusion in CEMs tend to outweigh the worse morphological (tortuosity) effects.

Figure 2.9b displays the relationship between micron-to-bulk tortuosity $\mathfrak{I}_{M-B}$ as a function of water content, which is clearly much smaller in both of CEMs and AEMs as compared to $\mathfrak{I}_{L-B}$. $\mathfrak{I}_{M-B}$ represents the degree of "disconnectivity" of water pathways, but only on the μm scale. This indicates that for many of these PEMs (especially the CEMs), the nm-scale to μm-scale heterogeneities (as indicated by the difference $\mathfrak{I}_{L-B} - \mathfrak{I}_{M-B}$) dominate over the larger scale heterogeneities ($\mathfrak{I}_{M-B}$). For AEMs on the other hand, we see that $\mathfrak{I}_{L-B} \approx \mathfrak{I}_{M-B}$, indicating that the hydrophilic cavities are very well connected below the μm scale. We believe this is the first instance of parsing the influence on bulk transport of subtle multi-scale heterogeneities. For such

random copolymer systems, we were surprised to find such strong effects due to $\mathfrak{I}_{M-B}$. We propose a basic model below that is consistent with these observations.

We note that these restricted diffusion observations contain information interpretable as the surface-to-volume ratio of the confined geometry, as shown by Mitra et al.[30, 38] This analysis is more complex and difficult to interpret in these random copolymer systems as compared to the above tortuosity analysis, and will form the basis of future restricted diffusion studies in polymer membranes. However, we have placed relevant information extracted from our fits of D_{H2O} to the Mitra equation in the Appendix.

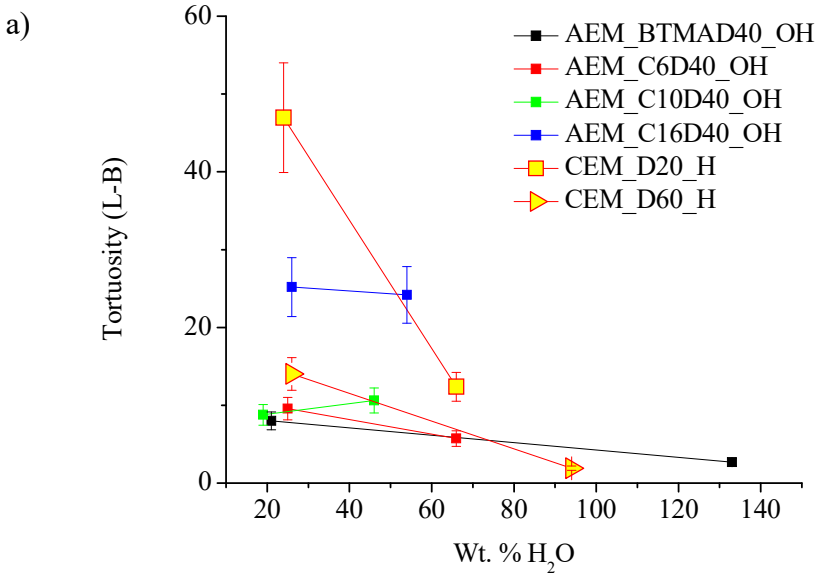

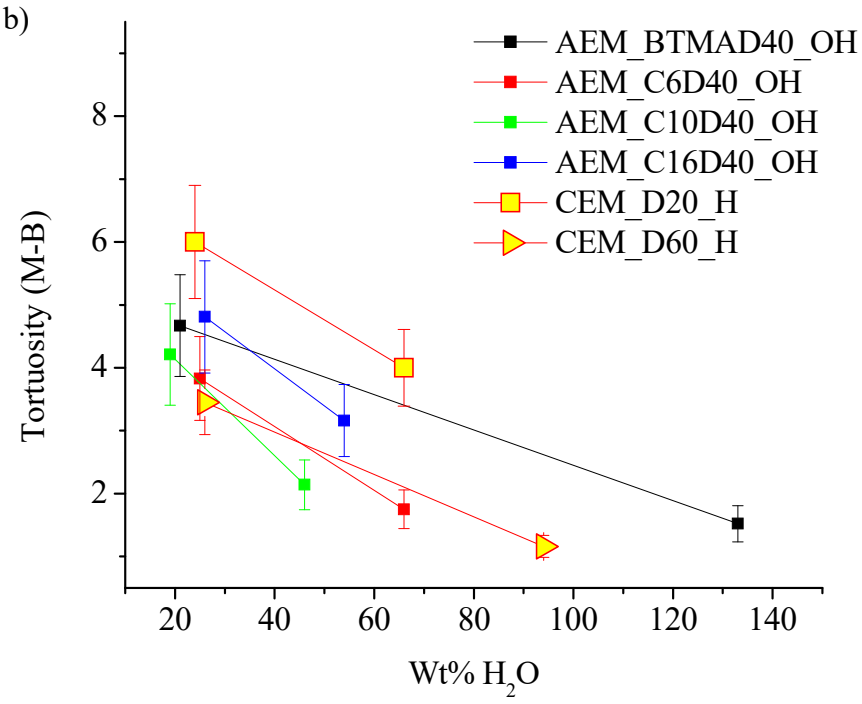

Figure 2.9. Tortuosity of AEMs and CEMs separated into two length scale ranges. a) Tortuosity from local to bulk ($\mathfrak{I}_{L-B}$). b) Tortuosity from micron to bulk ($\mathfrak{I}_{M-B}$). $\mathfrak{I}_{L-B}$ for CEMs is substantially higher than for AEMs (especially at low water content), indicating that while the connectivity (morphology) is worse than in AEMs, the local molecular water transport in CEMs is better. $\mathfrak{I}_{M-B}$ values are more similar among all membranes as compared to $\mathfrak{I}_{L-B}$, indicating higher dispersity in sub-μm morphological heterogeneities. Error bars for both tortuosity parameters are ±8% at high water content and ±15% at low water content.

Based on these tortuosity measurements and dependencies for these membranes, here we present a simple picture for the influence of water-content-dependent cavity connectivity on water transport (Figure 2.10). Figure 2.10a illustrates the nm-scale hydrophilic cavity network of PEMs at low, medium and high water content. At low hydration, the hydrophilic cavities (containing cluster of polymer-fixed ions and their associated counterions) are collapsed, resulting in a poorly interconnected hydrophilic network and slower overall bulk transport. At medium hydration, the hydrophilic cavities expand to fill up some "dead ends," resulting in a better interconnected network. At high hydration, the hydrophilic cavities grow even larger and more strongly connect the network. There are many dead ends at the nanometer scale, and the distance between each dead-end is of order a few nanometers. Figures 2.10b and 2.10c illustrate the consequences of more strongly interconnected networks, where dead ends must cluster together in some way so as to create micrometer-scale heterogeneity that is reflected in the NMR restricted diffusion observations ($\mathfrak{I}_{\mathrm{M-B}}$). At lower water uptake (Figure 2.10b), the hydrophilic network is more disconnected at the micrometer scale, leading to increased $\mathfrak{I}_{\mathrm{M-B}}$. At higher water uptake, the hydrophilic channels expands as in Figure 2.10a to connect many more of the dead ends, resulting in larger effective domain size and lower network tortuosity (Figure 2.10c). We are continuing to pursue more detailed NMR, scattering, and microscopy studies in order to understand the specific origin of the micrometer-scale heterogeneity that we ascribe here to clusters (boundary layers) of dead ends.

a)

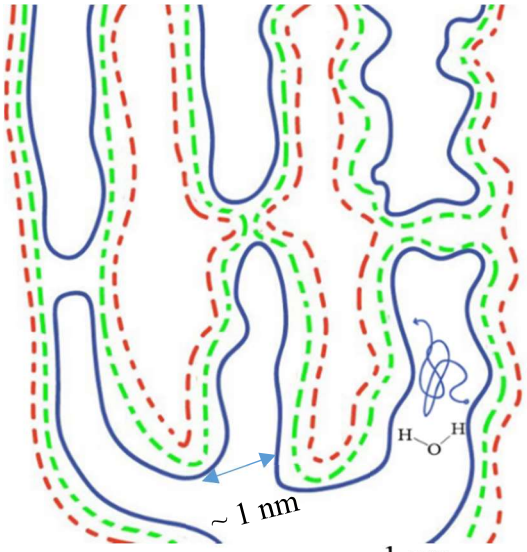

Low water uptake

Medium water uptake

High water uptake

b)

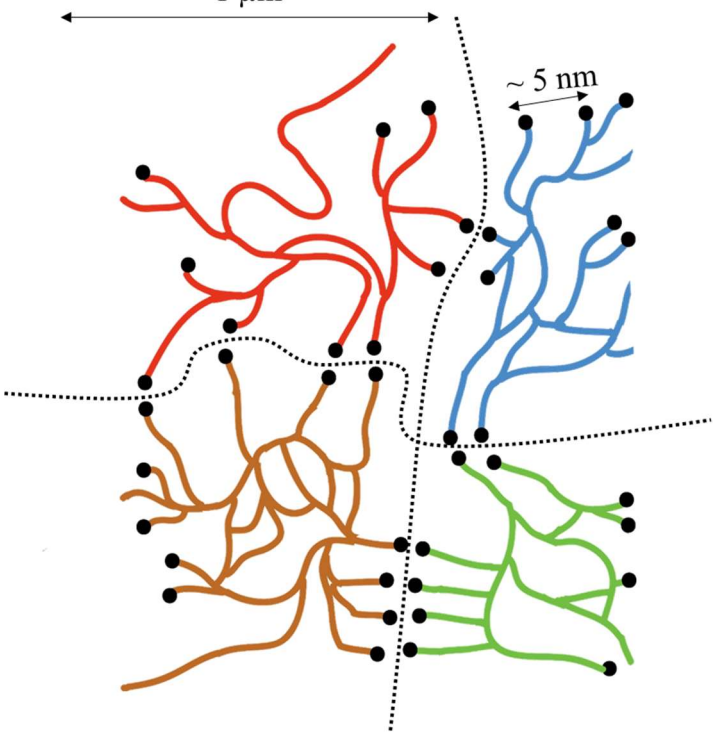

c)

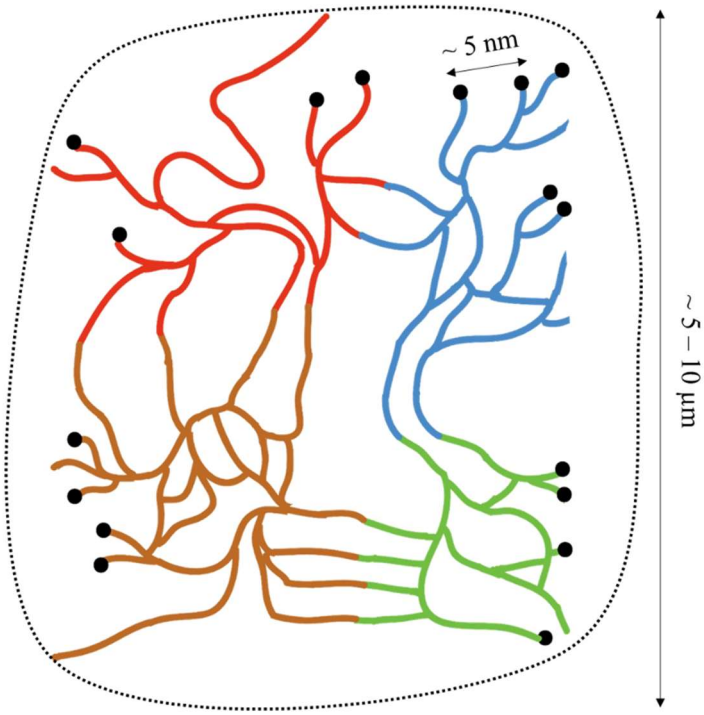

Figure 2.10. Model for multi-scale restricted water transport in AEMs and CEMs. a) Interconnected hydrophilic cavity network on the nanometer scale. The solid blue line represents the hydrophilic network at low hydration, the dashed green and red lines represent the network at increasing levels of hydration in which cavities become increasingly interconnected. b) Hydrophilic transport network with clusters of dead ends (black dots) that break overall connection pathways and create network domains on micrometer scales, as observed by NMR tortuosity measurements. This picture is idealized to show the concept, and of course this structuring would be much more irregular in terms of domain shape. That is, this structuring likely would not have spatial boundaries that consist of simple shapes such as squares, circles, ellipsoids, etc. At sufficiently long diffusion time Δ, water diffusion is restricted by these collections or boundary layers of dead-ends, leading to a decrease in D_{H2O} (restricted diffusion) and an increase in the tortuosity (both $\Im_{M-B}$ and $\Im_{L-B}$). At high water uptake, the hydrophilic cavities expand to connect many more dead ends to form open pathways, leading to decreased tortuosity of the network.

2.4. Conclusion

We have investigated water transport properties of a range of random copolymer cation-exchange and anion-exchange membranes (CEMs and AEMs) as a function of counterion type, alkyl sidechain length, and hydration level. Our detailed NMR diffusometry measurements demonstrate diffusion that can vary dramatically with composition, and with the length scale of the measurement. By plotting D_{H2O} as a function of water wt. % uptake, we gain more insight into how morphology affects transport. In a complementary way, by plotting D_{H2O} as a function of the water-ion mole ratio λ, we gain insight into how local intermolecular interactions affect transport. AEMs in particular show a common trend of water diffusion vs. water wt. % (but not vs. λ), indicating similar morphology across these membranes. Water diffusion in CEMs is generally faster than in AEMs, which arises from the faster local molecular transport effects in CEMs, even though from our studies AEMs exhibit more favorable morphology on scales larger than a few nm.

Based on varying the diffusion time Δ (and thus the length scale probed), we see restricted diffusion in all membranes. Furthermore, we introduce two separate tortuosity parameters, one averaged from nm-scale to bulk and one averaged from μm-scale to bulk, and these enable us to separately quantify the effects on transport of material heterogeneity on these different length scales. We introduce a model in the paper that is consistent with our tortuosity results and involves two parts: 1) Water swelling increases the local (nm-scale) connectivity of the hydrophilic cavities (e.g., bridging dead ends), which in turn decreases the tortuosity and increases bulk transport. 2) Heterogeneous clusters of pathway dead ends, which form effective boundaries to diffusion, are distributed such that there is a strong tortuosity effect observed on μm scales.

Extensions of this study are underway to gain more deep mechanistic information regarding the origins of the tortuosity and structural heterogeneities in these materials. Understanding the multi-scale phenomena that contribute to bulk water and ion transport in polymer membranes will help drive us toward the production of inexpensive and highly efficient membranes for fuel cells and a range of molecular separations.

Reference

1. Mauritz, K. A.; Moore, R. B., State of understanding of Nafion. *Chemical Reviews* **2004,** *104* (10), 4535-4585.
2. Elezovic, N. R.; Radmilovic, V. R.; Krstajic, N. V., Platinum nanocatalysts on metal oxide based supports for low temperature fuel cell applications. *Rsc Advances* **2016,** *6* (8), 6788-6801.
3. Chen, C.; Kang, Y. J.; Huo, Z. Y.; Zhu, Z. W.; Huang, W. Y.; Xin, H. L. L.; Snyder, J. D.; Li, D. G.; Herron, J. A.; Mavrikakis, M.; Chi, M. F.; More, K. L.; Li, Y. D.; Markovic, N. M.; Somorjai, G. A.; Yang, P. D.; Stamenkovic, V. R., Highly Crystalline Multimetallic Nanoframes with Three-Dimensional Electrocatalytic Surfaces. *Science* **2014,** *343* (6177), 1339-1343.
4. Li, X. M.; Hao, X. G.; Abudula, A.; Guan, G. Q., Nanostructured catalysts for electrochemical water splitting: current state and prospects. *Journal of Materials Chemistry A* **2016,** *4* (31), 11973-12000.
5. Shao, M. H.; Chang, Q. W.; Dodelet, J. P.; Chenitz, R., Recent Advances in Electrocatalysts for Oxygen Reduction Reaction. *Chemical Reviews* **2016,** *116* (6), 3594-3657.
6. Varcoe, J. R.; Slade, R. C. T.; Wright, G. L.; Chen, Y. L., Steady-state dc and impedance investigations of H-2/O-2 alkaline membrane fuel cells with commercial Pt/C, Ag/C, and Au/C cathodes. *J. Phys. Chem. B* **2006,** *110* (42), 21041-21049.
7. Hickner, M. A.; Herring, A. M.; Coughlin, E. B., Anion Exchange Membranes: Current Status and Moving Forward. *Journal of Polymer Science Part B-Polymer Physics* **2013,** *51* (24), 1727-1735.
8. Zhu, L.; Pan, J.; Wang, Y.; Han, J. J.; Zhuang, L.; Hickner, M. A., Multication Side Chain Anion Exchange Membranes. *Macromolecules* **2016,** *49* (3), 815-824.
9. Pan, J.; Zhu, L.; Han, J.; Hickner, M. A., Mechanically Tough and Chemically Stable Anion Exchange Membranes from Rigid-Flexible Semi-Interpenetrating Networks. *Chemistry of Materials* **2015,** *27* (19), 6689-6698.
10. Zhu, L.; Pan, J.; Christensen, C. M.; Lin, B. C.; Hickner, M. A., Functionalization of Poly(2,6-dimethyl-1,4-phenylene oxide)s with Hindered Fluorene Side Chains for Anion Exchange Membranes. *Macromolecules* **2016,** *49* (9), 3300-3309.
11. Zhu, L.; Zimudzi, T. J.; Li, N. W.; Pan, J.; Lin, B. C.; Hickner, M. A., Crosslinking of comb-shaped polymer anion exchange membranes via thiol-ene click chemistry. *Polymer Chemistry* **2016,** *7* (14), 2464-2475.
12. Mohanty, A. D.; Lee, Y.-B.; Zhu, L.; Hickner, M. A.; Bae, C., Anion Exchange Fuel Cell Membranes Prepared from C–H Borylation and Suzuki Coupling Reactions. *Macromolecules* **2014,** *47* (6), 1973-1980.
13. Jiao, K.; Li, X. G., Water transport in polymer electrolyte membrane fuel cells. *Progress in Energy and Combustion Science* **2011,** *37* (3), 221-291.
14. Li, J.; Park, J. K.; Moore, R. B.; Madsen, L. A., Linear coupling of alignment with transport in a polymer electrolyte membrane. *Nature Materials* **2011,** *10* (7), 507-511.
15. Hou, J. B.; Li, J.; Mountz, D.; Hull, M.; Madsen, L. A., Correlating morphology, proton conductivity, and water transport in polyelectrolyte-fluoropolymer blend membranes. *Journal of Membrane Science* **2013,** *448*, 292-299.

16. Li, J.; Wilmsmeyer, K. G.; Madsen, L. A., Anisotropic Diffusion and Morphology in Perfluorosulfonate Ionomers Investigated by NMR. *Macromolecules* **2009,** *42* (1), 255-262.
17. Hou, J.; Li, J.; Madsen, L. A., Anisotropy and Transport in Poly(arylene ether sulfone) Hydrophilic−Hydrophobic Block Copolymers. *Macromolecules* **2010,** *43* (1), 347-353.
18. Marino, M. G.; Melchior, J. P.; Wohlfarth, A.; Kreuer, K. D., Hydroxide, halide and water transport in a model anion exchange membrane. *Journal of Membrane Science* **2014,** *464*, 61-71.
19. Li, Y. S.; Zhao, T. S.; Yang, W. W., Measurements of water uptake and transport properties in anion-exchange membranes. *International Journal of Hydrogen Energy* **2010,** *35* (11), 5656-5665.
20. Hibbs, M. R.; Hickner, M. A.; Alam, T. M.; McIntyre, S. K.; Fujimoto, C. H.; Cornelius, C. J., Transport Properties of Hydroxide and Proton Conducting Membranes. *Chemistry of Materials* **2008,** *20* (7), 2566-2573.
21. Janarthanan, R.; Horan, J. L.; Caire, B. R.; Ziegler, Z. C.; Yang, Y.; Zuo, X. B.; Liberatore, M. W.; Hibbs, M. R.; Herring, A. M., Understanding Anion Transport in an Aminated Trimethyl Polyphenylene with High Anionic Conductivity. *Journal of Polymer Science Part B-Polymer Physics* **2013,** *51* (24), 1743-1750.
22. Li, N.; Leng, Y.; Hickner, M. A.; Wang, C.-Y., Highly Stable, Anion Conductive, Comb-Shaped Copolymers for Alkaline Fuel Cells. *Journal of the American Chemical Society* **2013,** *135* (27), 10124-10133.
23. Stejskal, E. O.; Tanner, J. E., SPIN DIFFUSION MEASUREMENTS: SPIN ECHOES IN THE PRESENCE OF A TIME-DEPENDENT FIELD GRADIENT. *Journal of Chemical Physics* **1965,** *42* (1), 288-292.
24. Tuckerman, M.; Laasonen, K.; Sprik, M.; Parrinello, M., Ab initio molecular dynamics simulation of the solvation and transport of hydronium and hydroxyl ions in water. *The Journal of Chemical Physics* **1995,** *103* (1), 150-161.
25. Lingwood, M. D.; Zhang, Z. Y.; Kidd, B. E.; McCreary, K. B.; Hou, J. B.; Madsen, L. A., Unraveling the local energetics of transport in a polymer ion conductor. *Chemical Communications* **2013,** *49* (39), 4283-4285.
26. Paddison, S. J.; Paul, R.; Zawodzinski, T. A., Proton friction and diffusion coefficients in hydrated polymer electrolyte membranes: Computations with a non-equilibrium statistical mechanical model. *Journal of Chemical Physics* **2001,** *115* (16), 7753-7761.
27. Chemical Rubber Company., CRC handbook of chemistry and physics. CRC Press.: Boca Raton, Fla. etc.
28. Zhang, J. H.; Giotto, M. V.; Wen, W. Y.; Jones, A. A., An NMR study of the state of ions and diffusion in perfluorosulfonate ionomer. *Journal of Membrane Science* **2006,** *269* (1-2), 118-125.
29. Hou, J.; Madsen, L. A., New insights for accurate chemically specific measurements of slow diffusing molecules. *The Journal of Chemical Physics* **2013,** *138* (5), 054201.
30. Price, W. S., Pulsed-field gradient nuclear magnetic resonance as a tool for studying translational diffusion: Part 1. Basic theory. *Concepts in Magnetic Resonance* **1997,** *9* (5), 299-336.
31. Barrie, P. J., Characterization of porous media using NMR methods. In *Annual Reports on Nmr Spectroscopy, Vol 41*, Webb, G. A., Ed. Elsevier Academic Press Inc: San Diego, 2000; Vol. 41, pp 265-316.

32. Valiullin, R., *Diffusion NMR of confined systems : fluid transport in porous solids and heterogeneous materials*. Royal Society of Chemistry: Cambridge, 2017; p xvii, 576 pages.
33. Shen, L.; Chen, Z. X., Critical review of the impact of tortuosity on diffusion. *Chemical Engineering Science* **2007,** *62* (14), 3748-3755.
34. Callaghan, P. T., *Translational dynamics and magnetic resonance : principles of pulsed gradient spin echo NMR*. Oxford University Press: Oxford ; New York, 2011; p xvii, 547 p.
35. Ohkubo, T.; Kidena, K.; Ohira, A., Determination of a Micron-Scale Restricted Structure in a Perfluorinated Membrane from Time-Dependent Self-Diffusion Measurements. *Macromolecules* **2008,** *41* (22), 8688-8693.
36. Yu, Z.; He, Y.; Wang, Y.; Madsen, L. A.; Qiao, R., Molecular Structure and Dynamics of Ionic Liquids in a Rigid-Rod Polyanion-Based Ion Gel. *Langmuir* **2017,** *33* (1), 322-331.
37. Wang, Y.; Chen, Y.; Gao, J. W.; Yoon, H. G.; Jin, L. Y.; Forsyth, M.; Dingemans, T. J.; Madsen, L. A., Highly Conductive and Thermally Stable Ion Gels with Tunable Anisotropy and Modulus. *Advanced Materials* **2016,** *28* (13), 2571-2578.
38. Mitra, P. P.; Sen, P. N.; Schwartz, L. M., Short-time behavior of the diffusion coefficient as a geometrical probe of porous media. *Physical Review B* **1993,** *47* (14), 8565-8574.

Appendix

Multiscale diffusion of water in CEMs and AEMs, and Mitra restricted diffusion analysis

In addition to the tortuosity analysis presented in Chapters 1 and 2 of this thesis, I also used a more complex model to analyze our diffusion coefficient data in all of the cation- and anion-exchange membranes. This Appendix summarizes that work, including more in-depth description of the commercial membrane Nafion®.

Nafion is a copolymer of tetrafluoroethylene with less than a 15% degree of ionic (sulfonate) side group functionalization.[1] Nafion draws significant attention as a cation exchange membrane (CEM) due to its excellent ion transport as well as superior thermal, chemical and mechanical stability.[2-4] Nafion's characteristic mainly comes from its well nanophase-separated morphology between the hydrophobic matrix and hydrophilic network.[1] Nafion has been broadly used as a reference sample for polymer electrolyte membranes (PEMs).[5-7]

The measurement of the diffusion coefficient of liquid molecules in a porous environment is critical because it can yield vital information about the morphology of porous environments such as sedimentary rocks, fuel-cell membranes, or human circulation.[8] As shown in Chapter 1, PFG NMR diffusometry can measure the self-diffusion coefficient of liquid molecules.[9] Mitra and his coworker have quantitatively developed a model to extract the surface area to volume ratio of micro geometry from the dependence of diffusion coefficient on diffusion time.[10] Besides, Mitra also developed a theory about the "diffraction-like behavior" of spin echo amplitude in long diffusion time to reveal the information of pore connectivity.[11-12] Although the "diffraction-like behavior" phenomenon is fascinating; it is beyond the scope of this work.

Theoretically, Nafion can be considered as a porous material, in which, hydrophobic part is a solid matrix providing mechanical structure, and the hydrophilic network provides the pores for water and ion transport. We applied Mitra theory of restricted diffusion to explore this behavior in Nafion membranes, following and expanding on previous work.[13] Nevertheless, due to the initial nature of our understanding of morphology in these random copolymer PEMs, our Mitra analysis requires further development for a complete PEM transport-morphology model. Thus, I have decided to focus on tortuosity arguments and not to incorporate the more complex Mitra analysis.

According to Mitra, in short diffusion time, a certain fraction of the particles will feel the effects of the boundary. The diffusion coefficient, thus, will contain the information surface-to-volume ratio of the confined geometry as shown in Eq. 1.[10]

$$\frac{D(t)}{D_0} \approx 1 - \frac{4}{9\sqrt{\pi}}\sqrt{D_0 t}\,\frac{S}{V} + \varphi\,(\rho, R, T) \quad (1)$$

Where D (t) is the diffusion coefficient varied with the diffusion time, D_0 is the bulk diffusion coefficient, t is the diffusion time, S/V is the ratio of surface area to volume. $\varphi\,(\rho, R, T)$ is the deviation due to the finite surface relaxivity and curvature (R) of the surfaces.

From the Mitra equation, we can derive the surface area to volume ratio and D_0. D_0 in this case nevertheless is not the diffusion coefficient of bulk water because it is from three to thirty times smaller. Ohkubo and his coworker proposed a 2-step diffusion attenuation to explain the behavior of water in Nafion as illustrated in Figure A1.[14] Before water molecules hit the wall of the nanometer hydrophilic channel, the diffusion coefficient of water remains as the bulk diffusion (the diffusion time is in the order of ps). When the diffusion length of water molecules exceeds the diameter of the channel, its diffusion coefficient decreases until it reaches D_0. According to Ohkubo, D_0 reflects the diffusion within the homogeneous network of channel and contains

information about tortuosity. When diffusion time increased to ms, the diffusion coefficient of water kept decreasing until it reached equilibrium. There may be two factors contributing to the attenuation of the diffusion coefficient as the tortuous cavity diffusion distance (for the attenuation at nm scale) and the cavity network diffusion distance (for the attenuation at μm scale)

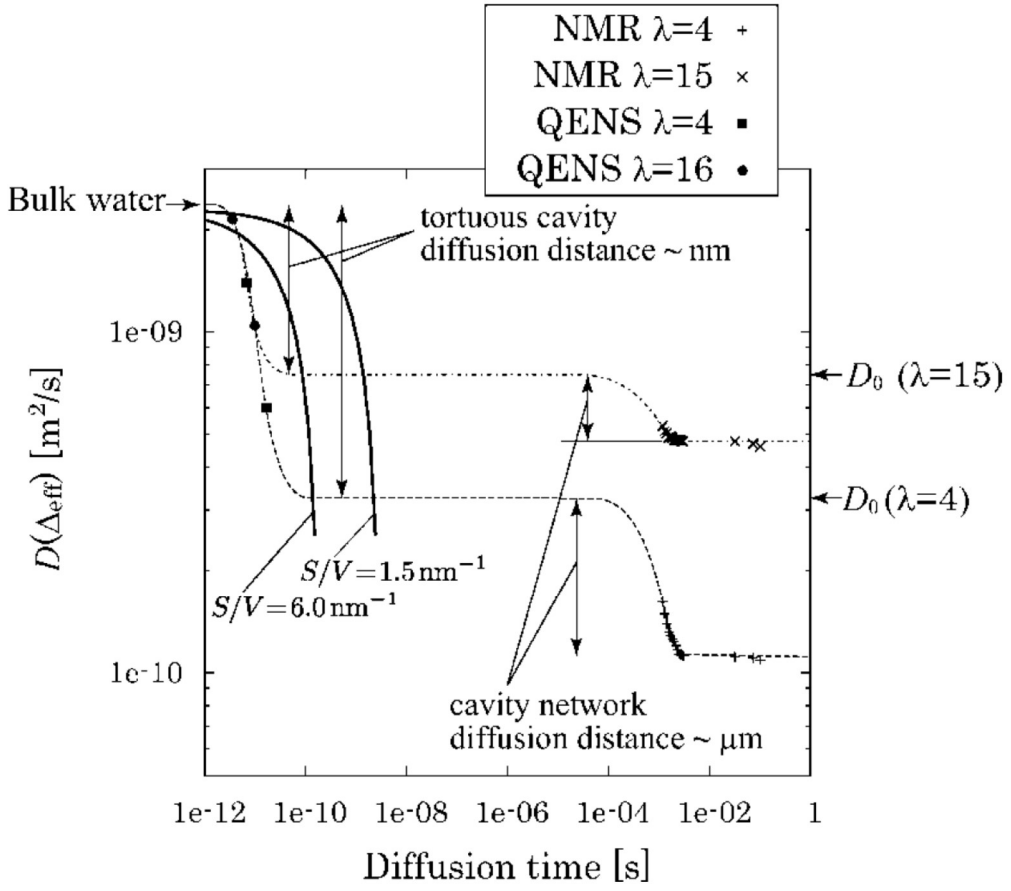

Figure A1. Multiscale diffusion of water in Nafion. There is 2-steps diffusion timescale, one in the order of ps and one is in the order of ms. D_0 reflects the diffusion within the homogeneous network of channel and contains information about tortuosity. There may be two-factor contributing to the attenuation of the diffusion coefficient as the tortuous cavity diffusion distance (for the attenuation at nm scale) and the cavity network diffusion distance (for the attenuation at μm scale). Figure reproduced from Ohkubo et al.[14]

Surface area to volume ratio and R_c derived from Mitra equation

The Mitra equation has been applied broadly to study the morphology of porous material. If we use water as the molecular probe and measure the diffusion time in 1 ms, apparent diffusion length would be ~ 1.5 μm, about the pore size of the conventional porous molecule.

Theoretically, we also can consider AEMs and CEMs as a porous material, in which, hydrophobic part is a solid matrix providing mechanical structure, and the hydrophilic channel provides the pores for water and ion transport. Nevertheless, the hydrophilic channel of PEMs is on the order of one or a few nanometers, which would require a PFG NMR diffusion time on the order of nanoseconds, which is too small a time scale to reach with PFG NMR.

To overcome this limitation, we can consider the micrometer structure of PEMs as the assemblage of thousands of nanometer-scale channels. D_0 is now the diffusion coefficient average over ~ 1 nm pathways structure, representing the homogeneity in micrometer. Eq. 1 is then valid for "short time" region for PFG-NMR diffusometry. It is noted that the definition of short time is relative in here. At low water content, the hydrophilic domain shrinks, the "short" length scale is about ~ 2 – 5 μm. However, at saturated water content, the hydrophilic channel absorbs water to expand, the "short" length scale may rise to 10-15 μm. Figure A2 shows the average domain size of AEMs and CEMs at the saturated water content and same water content. All this information is summarized in Table A1.

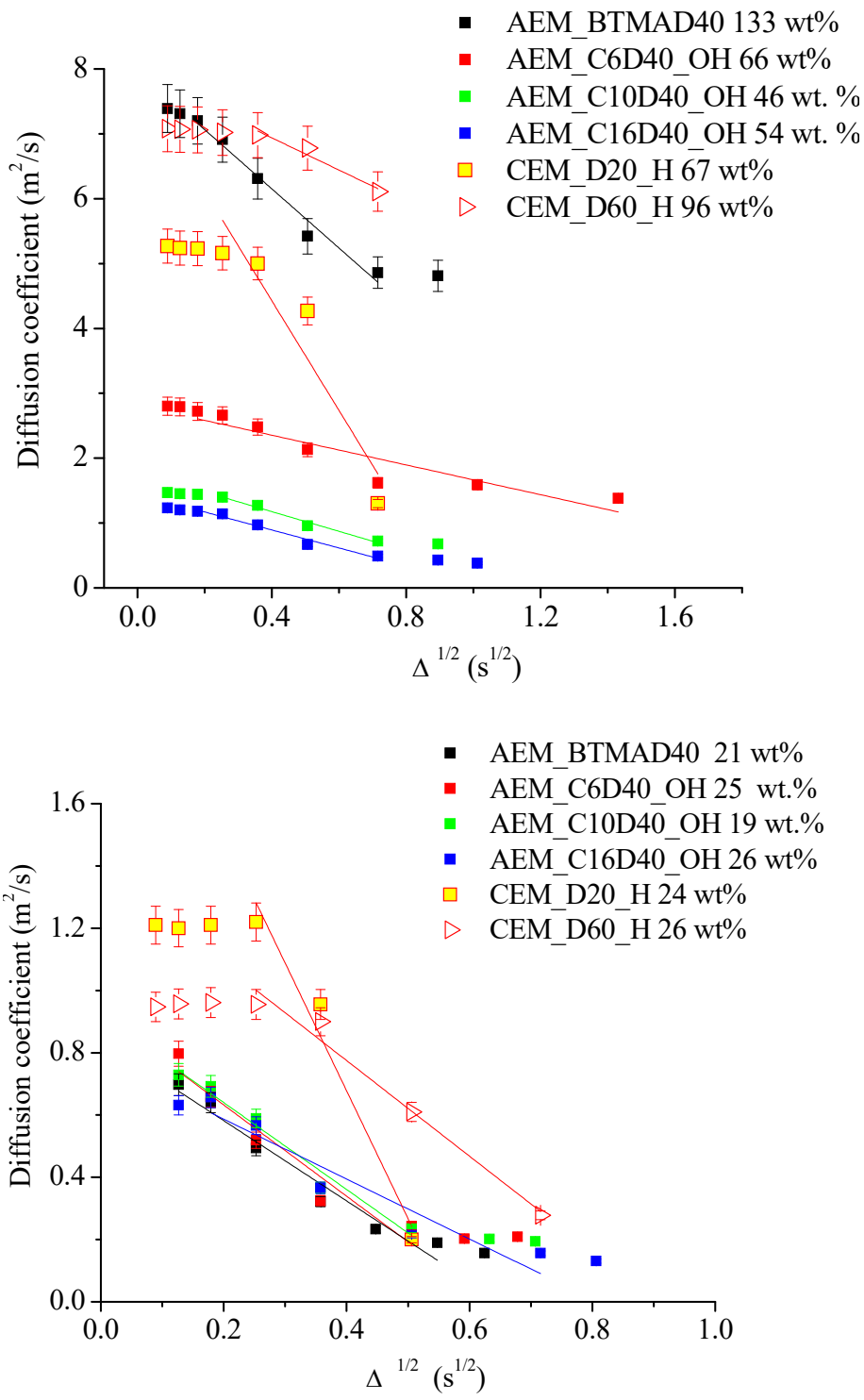

Figure A2. Diffusion coefficient vs. diffusion time square root of AEMs and CEMs at a) saturated water uptake b) similar water uptake. Error bars for diffusion coefficient measurement are ≤ ±5%

Table A1. Average domain size information

	wt. % H_2O	R_c (x 10^{-5} m)	S/V (x 10^5 m^{-1})
AEM_BTMA_OH	133.0	1.24	0.81
AEM_BTMA_OH	21.0	0.15	6.60
AEM_C6_OH	66.0	1.04	0.97
AEM_C6_OH	25.0	0.15	6.50
AEM_C10_OH	46.0	0.39	2.60
AEM_C10_OH	19.0	0.16	6.30
AEM_C16_OH	54.0	0.31	3.20
AEM_C16_OH	26.0	0.18	5.60
CEM_D20_H	66.0	0.84	1.20
CEM_D20_H	24.0	0.08	12.0
CEM_D30_H	29.0	0.18	5.70
CEM_D30_H	24.0	0.10	9.60
CEM_D40_H	42.0	0.24	4.10
CEM_D40_H	26.0	0.17	6.0
CEM_D50_H	67.0	0.91	1.10
CEM_D50_H	24.0	0.17	6.0
CEM_D60_H	94.0	1.90	0.50
CEM_D60_H	26.0	0.15	6.60

References

1. Mauritz, K. A.; Moore, R. B., State of understanding of Nafion. *Chemical Reviews* **2004,** *104* (10), 4535-4585.
2. Li, J.; Park, J. K.; Moore, R. B.; Madsen, L. A., Linear coupling of alignment with transport in a polymer electrolyte membrane. *Nature Materials* **2011,** *10* (7), 507-511.
3. Li, J.; Wilmsmeyer, K. G.; Madsen, L. A., Anisotropic Diffusion and Morphology in Perfluorosulfonate Ionomers Investigated by NMR. *Macromolecules* **2009,** *42* (1), 255-262.
4. Peighambardoust, S. J.; Rowshanzamir, S.; Amjadi, M., Review of the proton exchange membranes for fuel cell applications. *International Journal of Hydrogen Energy* **2010,** *35* (17), 9349-9384.
5. Lingwood, M. D.; Zhang, Z. Y.; Kidd, B. E.; McCreary, K. B.; Hou, J. B.; Madsen, L. A., Unraveling the local energetics of transport in a polymer ion conductor. *Chemical Communications* **2013,** *49* (39), 4283-4285.
6. Hou, J.; Li, J.; Madsen, L. A., Anisotropy and Transport in Poly(arylene ether sulfone) Hydrophilic−Hydrophobic Block Copolymers. *Macromolecules* **2010,** *43* (1), 347-353.
7. Park, J. K.; Li, J.; Divoux, G. M.; Madsen, L. A.; Moore, R. B., Oriented Morphology and Anisotropic Transport in Uniaxially Stretched Perfluorosulfonate Ionomer Membranes. *Macromolecules* **2011,** *44* (14), 5701-5710.
8. Mitra, P. P.; Latour, L. L.; Kleinberg, R. L.; Sotak, C. H., Pulsed-Field-Gradient NMR Measurements of Restricted Diffusion and the Return-to-the-Origin Probability. *Journal of Magnetic Resonance, Series A* **1995,** *114* (1), 47-58.
9. Stejskal, E. O.; Tanner, J. E., SPIN DIFFUSION MEASUREMENTS: SPIN ECHOES IN THE PRESENCE OF A TIME-DEPENDENT FIELD GRADIENT. *Journal of Chemical Physics* **1965,** *42* (1), 288-292.
10. Mitra, P. P.; Sen, P. N.; Schwartz, L. M., Short-time behavior of the diffusion coefficient as a geometrical probe of porous media. *Physical Review B* **1993,** *47* (14), 8565-8574.
11. Mitra, P. P.; Sen, P. N., Effects of microgeometry and surface relaxation on NMR pulsed-field-gradient experiments: Simple pore geometries. *Physical Review B* **1992,** *45* (1), 143-156.
12. Mitra, P. P., Diffusion in porous materials as probed by pulsed gradient NMR measurements. *Physica A: Statistical Mechanics and its Applications* **1997,** *241* (1), 122-127.
13. Hou, J. B.; Li, J.; Mountz, D.; Hull, M.; Madsen, L. A., Correlating morphology, proton conductivity, and water transport in polyelectrolyte-fluoropolymer blend membranes. *Journal of Membrane Science* **2013,** *448*, 292-299.
14. Ohkubo, T.; Kidena, K.; Ohira, A., Determination of a Micron-Scale Restricted Structure in a Perfluorinated Membrane from Time-Dependent Self-Diffusion Measurements. *Macromolecules* **2008,** *41* (22), 8688-8693.